Calibration of ILIDS and PDPA droplet sizing systems and their application to the breakup of impacting water and air jets

Sebastian Kosch, University of Toronto

2015

List of symbols and abbreviations

$\Delta\vartheta$	Angular spacing between two adjacent fringes
Δz	Distance along the z-axis between the focal plane of the lens and the light sheet
$\hat{N}_{\mathrm{fr}}$	Peak fringe count measured
$\varkappa$	Scalar value relating the fringe count N_{fr} to the physical diameter of the particle D_d
D_{i}	Diameter (in pixels) of the defocussed image
D_{padded}	Width (in pixels) of the padded input to the Fourier transform
D_d	Physical diameter of the particle (here: droplet)
$d_{p,x}$; $d_{p,y}$	Physical dimensions of a pixel on the camera's CCD sensor
f_{peak}	Peak frequency
M	Magnification
N_{fr}	Number of fringes
s_x	Distance, in pixels, between two adjacent fringes

Introduction

1.1 Why spray sizing is important

1.2 What our contributions in this paper are

- Our contributions: - Pupillary magnification has to be taken into account - Circle detection algorithm is crap

1.3 What other work has been done in this area

Experimental setup

- What kinds of setups there are
    - Our setup:

2.1 Dantec system

- Dantec system

2.2 PDPA system

- TSI system

Monodisperse droplet generation

To calibrate any droplet sizing device, we need droplets of known and uniform size. Sprays or streams of such uniform droplets are called *monodisperse*, and many different varying approaches to generating them have been proposed, each one with advantages and drawbacks.

The most basic type of droplet generator is a capillary tube, for instance a hypodermic needle or a pulled glass pipette. Droplets are generated as the liquid flows through the tube due to its own weight. As the liquid leaves the tube, it wets the tip of the tube and forms a bead held together by surface tension. Eventually, the bead's gravitational forces overcome the attraction to the tube surface, and the drop separates from the tube.

Given a liquid and its physical properties, the only remaining controllable variable is the diameter of the capillary tube tip. As a rule, droplets generated in this fashion will be significantly larger than the tube diameter from which they grow. Most droplet generators are designed to prevent this from happening:

- *Aerodynamic* droplet generators use coaxial air flow to shear the forming droplet off of the capillary tip before it can grow to full size.
- *On-demand* droplet generators use a pressure pulse to eject a fixed amount of liquid out of the capillary (or other orifice).
- *Continuous-stream* droplet generators use mechanical vibrations to break up a continuous jet of liquid emanating from the capillary into monodisperse droplets.

More exotic types of droplet generators exist: Walton and Prewett [1] suggested that water falling on spinning disks is propelled outwards, forming nearly monodisperse droplets, and several improved designs have been published since. Another approach, e.g. used by Merritt and Drinkwater [2], involves mechanized dipping of a needle into a liquid reservoir, and then flicking it so as to produce one droplet.

3.1 Aerodynamic droplet generators

Allan et al. [3] provide a history of aerodynamic designs: the first design was published in 1947 by Lane [4]; Reil and Hallett [5] later improved on it by using time-controlled air pulses instead of a continous flow. Coggins and Baker [6] have proposed a more elaborate apparatus with variable air and liquid flow and adjustable needle position.

3.1.1 Stry design

Initial tests based on a design by Stry [7] showed that the ability of the instrument to produce droplets below 600 μm depends entirely on the precision with which the flow of water and air can be controlled.

3.2 On-demand drop generators

Drop-on-demand technology finds its most important application in printing. Indeed, the most prominent designs representative of this category are the thermal droplet generators found in most household inkjet printers, invented by Endo et al. [8]. At least one research group, Sergeyev and Shaw [9], has succeeded in repurposing an old inkjet print head for laboratory droplet generation.

Less widespread, but more flexible in a research setting, are on-demand generators driven by the contraction of piezoelectric elements, such as those proposed by Yang et al. [10] or Ulmke et al. [11]. Excellent reviews on drop-on-demand designs were published by Le and Lee [12, 13].

A curious third type of on-demand generator by Amirzadeh Goghari and Chandra [14] uses a short pulse of pressurized air, controlled by a solenoid valve, to eject a small amount of liquid through an orifice.

While drop-on-demand generators are a crucial component in applications like inkjet

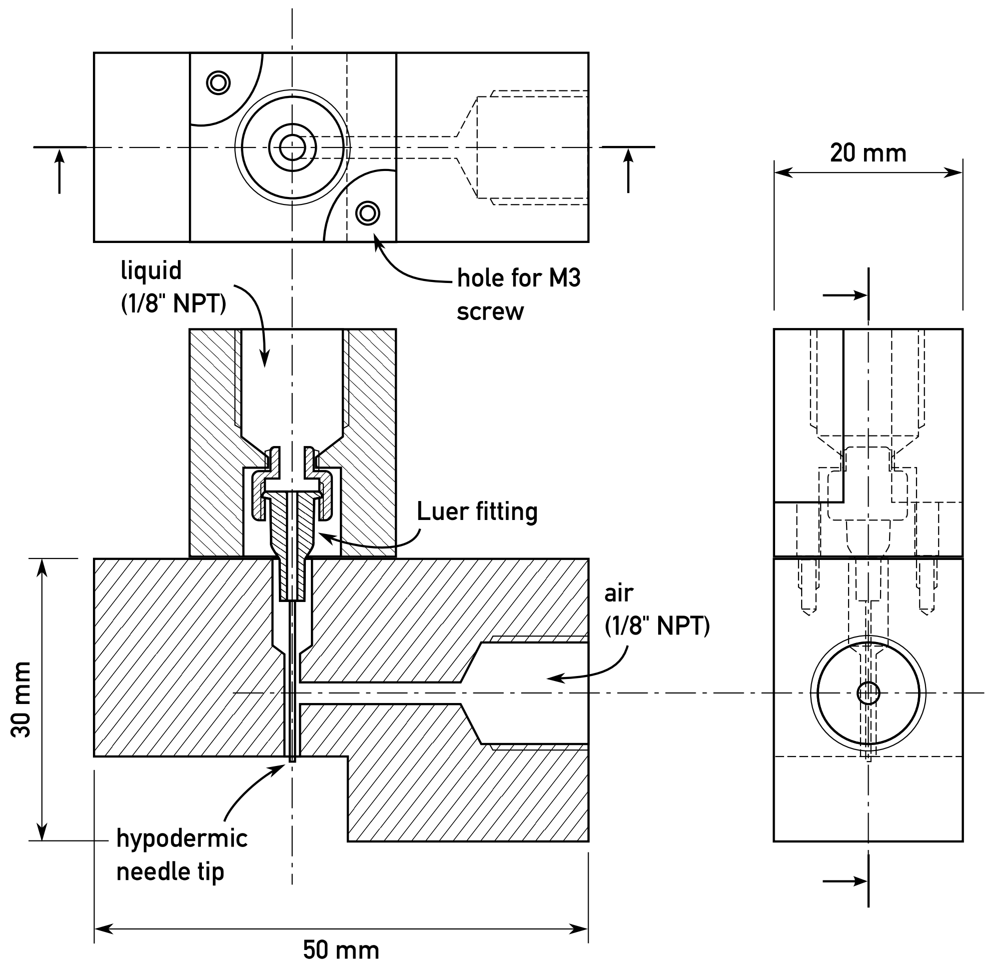

Figure 3.1: Schematic drawing of the coaxial-flow aerodynamic droplet generator, based on Stry [7]. Top: top view, right: rear view (third angle projection). Sectional view illustrates operating principle.

printing or microfluidics, they tend to suffer from aspired air bubbles, pileup of liquid around the nozzle tip, clogging, and other issues thwarting reliable drop expulsion unless manufactured and operated with great attention to detail.

3.2.1 Amirzadeh Goghari and Chandra design

We constructed a droplet generator based on the design by Amirzadeh Goghari and Chandra [14]. While both its construction from off-the-shelf parts and its operation are remarkably straightforward, it has two limitations:

— the duration of the air pulse is limited by the response time of the solenoid valve used. The shortest pulse we were able to reliable produce was on the order of a few milliseconds, which did not permit us to produce droplets smaller than a few hundred microns in diameter, and

— the head of water over the orifice must be kept very low to prevent leakage. As a result, the number of droplets that can be ejected is limited before the water needs to be replenished.

Owed to our lack of access to an automatic micropipette puller, the nozzles used in this experiment were not optimal, which likely contributed to our experience of frequent satellite droplets and liquid buildup at the nozzle tip.

3.2.2 Modified Yang design

A popular piezoelectric-based drop-on-demand design was proposed by Yang et al. [10]. It consists of a liquid-filled chamber, one wall of which is the underside of a piezoelectric disk—a brass disk coated with a circular piece of piezoelectric material, commonly found in electric buzzers.

To evaluate the performance of such a drop generator, we constructed several modifications of it, the final one of which is shown in Fig. 3.2. To make the chamber as flat as possible, minimizing the distance between piezoelectric disk and orifice, it has a depth of only about 2.5 mm, the thickness of a sheet of acrylic. A second sheet holds the disk in place, while a third sheet makes up the bottom wall of the chamber. Nozzle and inlet are glued directly into the bottom sheet.

To operate the droplet generator, water is fed through the inlet port until the chamber is filled and all air bubbles have escaped through the upward-facing nozzle. The generator

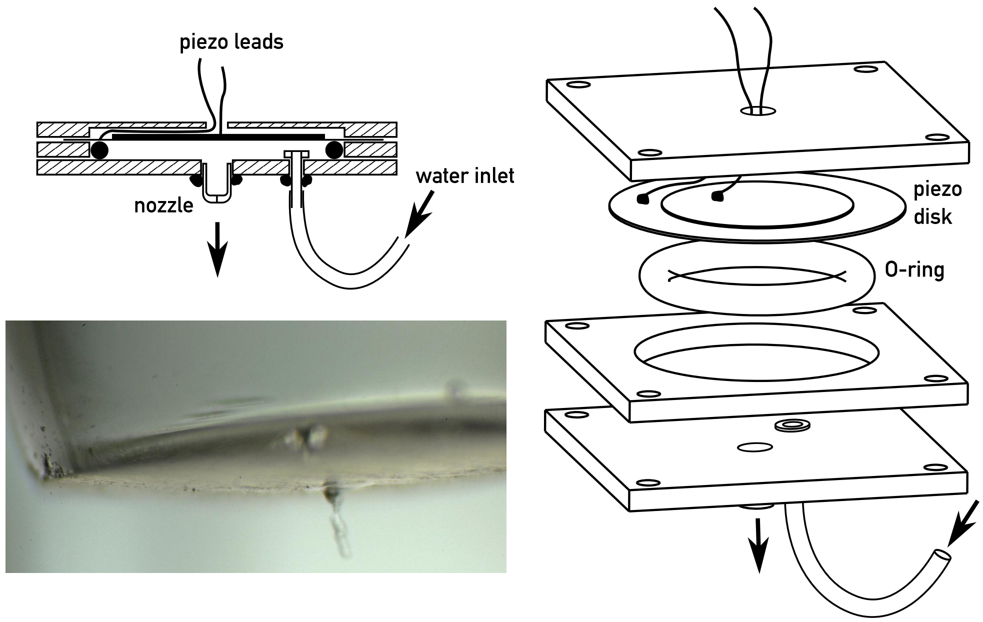

Figure 3.2: Top and right: schematic cross-section and exploded view of our piezoelectric droplet generator. Bottom left: photomicrograph of the nozzle tip ejecting a column of water (diameter $\approx 125\,\mu$m), which is about to coalesce into a round droplet.

is then turned so that the nozzle faces down and 30 ms pulses of about 30 V are delivered to the piezoelectric disk.

The greatest challenge faced was the accumulation of liquid on the nozzle surface, which quickly led to satellite droplets or thwarted droplet production altogether.

Again, capillaries drawn with an automatic pipette puller are likely more resistant to this effect.

3.2.3 Piezo-based drop generator

We tried building a Piezodropper from old piezoelectric elements squeezing glass capillaries (just like in the Ulmke paper), but two of the piezo elements were broken, and the third one had a capillary that clogged up repeatedly. We abandoned the approach before building a functioning droplet generator, although it seems attractive in practice. One downside is that the generation of amplified signals isn't straightforward – we used a soundcard connected to an amplifier to generate the signals.

3.3 Continuous-stream drop generation

There exist continuous-stream drop generators based on coaxial air flow [15] and on, but most continuous-stream drop generators are based on *Rayleigh breakup*, i.e. the disintegration of a disturbed liquid jet into droplets. The physics behind this phenomenon have been studied for almost two centuries [16, 17] and are well-understood. When the jet disturbances are induced by carefully controlled mechanical vibrations at an appropriate frequency, the droplets will be of uniform size and evenly spaced.

This simple principle has been employed to generate droplets for fifty years, with orifices typically attached to either one of two vibrating mechanisms: an ordinary loudspeaker, first used by Donnelly and Glaberson [18], or a piezoelectric element, as first proposed by Schneider and Hendricks [19] and popularized by Berglund and Liu's design [20].

3.3.1 Speaker-based drop generator

We used a big plastic underwater woofer, with a bendable metal strap taped to the cone. The end of the metal strap touched and vibrated the nozzle. At large droplet sizes, this is no problem at all, but once we get to about 1 kHz, the amplitude needs to go up considerably to yield a reliable breakup. In practice, this means that it gets very loud, jeopardizing the laboratory peace.

3.3.2 Hard-drive based drop generator

The accuracy of the hypodermic needle nozzle often isn't quite as good as that of e.g. photofabricated nozzles, as those have sharp edges. The round edges lead to variability in discharge coefficient (and mass flow), resulting in variance in drop volume [21]. Nevertheless, for the purpose of verifying the validity of measurements, it'll do.

Both speaker-based and piezo-based approaches have certain drawbacks: by design, a speaker vibrating at a fixed pitch produces an audible sound, jeopardizing the laboratory peace. Speakers are unshapely, difficult to fasten onto an experimental setup and their cones provide no robust structure to which any type of orifice could be attached. Piezoelectric elements cost more and are useful only when integrated with the orifice—precision machined droplet generators operating this way are commercially available, but unreasonably expensive in many situations. As a result, we felt compelled to consider alternative sources of vibration that require a minimum effort to build and install using standard lab equipment, and chose the actuator mechanism found in every magnetic hard drive for the following properties:

Very low cost. With high-capacity and solid-state devices rapidly pushing older hard drives into obsolescence, it should be a simple matter to acquire a few decommissioned specimens for demolition. Hard drives come in two form factors—3.5 and 2.5 inches wide, respectively—and both can be used for the purposes of this paper.

Further, glass needle orifices fabricated for use with existing loudspeaker setups can be reused, and are easily produced by hand from heated borosilicate capillaries or using a micropipette puller. The process is illustrated in Fig. 3.3 and in-depth instructions are given by Lee[13]. Piezoelectric-based devices, on the other hand, need fitted orifices to produce a range of drop sizes.

Ease of construction and installation. Unlike loudspeakers, hard drives have a flat base plate which can be drilled into, allowing for easy installation on any experiment jig. Save for a drill and a saw, no machining tools are needed for the construction of the droplet generator.

High amplitudes without noise. Like piezoelectric elements, vibrating actuator arms are very quiet, enabling use at frequencies and amplitudes that would far exceed responsible levels on a speaker. In our experiments, the actuator responded to frequencies throughout our hearing range—i.e., up to 17 kHz—and likely well beyond, though we have not tested the full response range for any given amplitude.

As an added advantage over other designs, no amplification is needed. Below 100 Hz, amplitudes on the order of 0.5 cm are easily achieved (albeit they are of course not needed for droplet production) when a peak-to-peak voltage of $2-4$ V is applied. The amplitude scales down with the inverse of the frequency, however, such that amplitudes are much smaller at typical operating frequencies ($0.5-10$ kHz). Nevertheless, the voltages required are well within the ability of any standard laboratory function generator, and can likely even produced by many consumer-level computer sound cards.

Operating principle

Magnetic hard drives store data as sub-micron-sized patterns of oppositely magnetized dots on disks called *platters*. The read-write head is mounted at the tip of an arm that pivots across the platter surface while the platter spins. This setup allows the head to access the entire platter surface.

Fig. 3.4b illustrates schematically the design of a typical actuator arm assembly. The flat voice coil mounted on the surface is responsible for the arm's side-to-side movement: as it is positioned under a permanent magnet, the coil creates a sideward force when a current flows through its wires. By stopping or reversing the current the arm's motion is likewise stopped or reversed. Since a typical hard drive's platter spins at up to 7200 RPM, actuator arms must be able to move with extreme speed and precision. They are thus engineered to be very light yet stiff. These characteristics make a magnetic hard drive's actuator arm an ideal supplier of in-plane vibrations. Indeed, hard drive actuators are remarkable not for their operating principle but for their low cost; it is only the economics of mass manufacturing that has in recent years enabled these high-speed, lightweight precision mechanisms to become so widely available.

Construction

If possible, forgo multi-platter drives, as they are more cumbersome to disassemble and have bulky, complex actuator assemblies. The device shown in Fig. 3.4a is based on a single-platter drive.

Dismantle and cut. After removing the hard drive cover, remove the magnet holder, arm axis, arm, ribbon wires, circuit boards, and platters such that only the base plate remains. Now the corner of the base plate holding the actuator arm assembly can be cut out to yield the result shown in Fig. 3.4b. A band saw, jigsaw or powered hacksaw will be very useful, although

Figure 3.3: Above: assembly of nozzle from low-gauge hypodermic syringe (Luer fitting) and capillary. Below: nozzle tip fabrication, capillary from left to right: broken, sanded, heated in a flame (I.D. 200 μm), heated for longer (I.D. 25 μm, could be sanded down by about 200 μm), overheated (I.D. 0 μm).

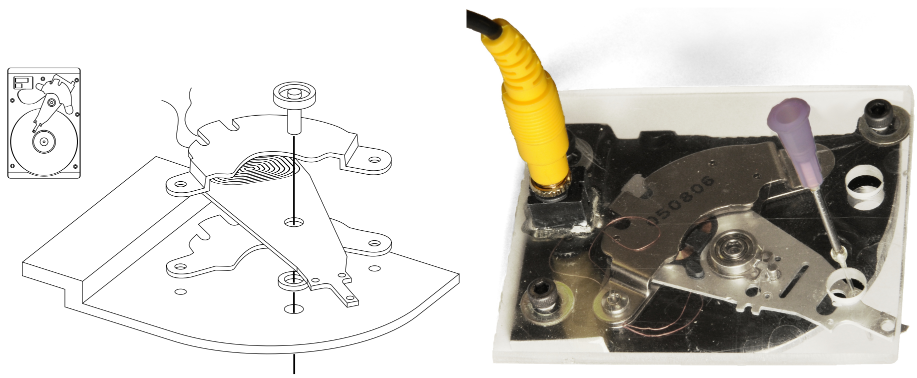

(a) (b)

Figure 3.4: (a) top view of a hard drive and exploded view of the cut-out base plate, actuator arm, axis, and magnet assembly; (b) assembled droplet generator with cover plate and nozzle inserted through actuator arm.

not necessary. The goal is to allow the tip of the arm to protrude over the edge.

Expose coil leads. Next, remove the read/write head and all wiring leading to it, along with any connected I/O and servo circuitry. Be careful, however, not to tear off the two strands powering the voice coil. If they are integrated in a ribbon you wish to remove, ensure that exposed terminals remain onto which you can solder new leads.

Add protective cover. We recommend bolting on a cover plate, such as a small sheet of acrylic or polycarbonate, to protect the protruding arm from accidental bending. Drill a hole through the cover to allow the nozzle to be threaded through the arm. A severable connection from coil to function generator is preferable to a direct wire, if only because the voice coil leads are delicate and easily torn off. To this end, we epoxied an audio jack into the cover and soldered the voice coil leads to it from the bottom.

Operation

To use the droplet generator, simply insert a nozzle through a small hole at the tip of the actuator arm—typically at least one hole will already be present, but you may wish to drill more—and connect the voice coil leads to the output terminal of a function generator set to an initial peak-to-peak voltage of 1 V and a sinusoid frequency of about 50 Hz, which should cause weak but perceptible oscillations.

We used existing nozzles manufactured by hand from hypodermic needle stubs and heated glass capillaries (Fig. 3.3). We make no claim that this is the best approach to take, but we note that the interchangeability of nozzles with Luer fittings has proved very convenient in our application. How the nozzle can be held in place falls beyond the scope of this article; while we used an existing setup made from machined aluminum, a small lab stand and clamp should suffice to hold the male Luer fitting connecting the feed tube to the nozzle.

The nozzle must be supplied by an accurately calibrated syringe pump. It is convenient to integrate a large liquid reservoir (or tap water hose) via a T-valve between the between pump and nozzle to permit quick topping up of the syringe. In such a setup ensure that the reservoir valve is shut closed before operation, since pressure fluctuations at the nozzle are the most common culprit for unstable jet breakup conditions.

As with other vibrating orifice droplet generators, it is crucial that stable conditions are established before any experiments can begin. First, confirm that the liquid is ejected in a single jet. Multiple jets can be due to a clogged orifice (a mixture of distilled water and CLR®, drawn back through a syringe, is an excellent remedy). Satellite droplets can also form secondary jets, in which case the oscillation frequency must be adjusted or the amplitude reduced. Satellite formation is easily detected by using a gentle air flow to deflect the jet—if the droplets are truly monodisperse, they will all deflect at the same angle.[22]

3.4 Determining the produced droplet size

With droplet generators based on Rayleigh breakup, such as the HDG, this is easy to do; just take the flow rate and divide by the number of droplets produced per second (which, under stable conditions, equals the vibration frequency as each instability turns into one droplet). If we assume perfect sphericity, we can convert this droplet volume into a diameter. After cancelling terms, the expression for D_d becomes

$$D_d = \sqrt[3]{\frac{6Q}{\pi f}} \tag{3.1}$$

The reliablity of the underlying assumption has been verified photographically for several different nozzle orifice diameters and frequencies, some of which are given as part of the ILIDS calibration.

3.4.1 Photographing droplets

With drop-on-demand approaches, the diameter of the produced droplet is more difficult to predict, particularly since not the whole squeezing volume may result in ejected liquid (e.g. with the Chandra generator, it's just a small droplet). So to find out how big these droplets are (or just to verify the accuracy of Eq. (3.1)), we must resort to photographic means.

While there are different methods of photographing droplets, just taking pictures in front of a strobe light has worked well.

We used a scale placed next to the droplet stream, and then used a conversion between pixels to find the size. Of course, this method suffers from barrel distortion that inevitably happens, especially with a zoom lens. Figure X shows a typical droplet stream photo (at different sizes).

3.4.2 Droplet collisions

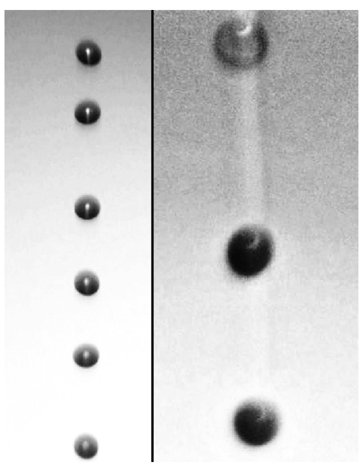

Figure 3.5: Photographs of different droplet sizes (220 μm and 386 μm, $f = 1.990$ kHz and 1.065 kHz respectively) produced with the droplet generator shown in Fig. ??. Scales have been cropped out.

No droplet generation mechanism is perfect. Small fluctuations in flow rate, unwanted harmonic vibrations and air turbulence can cause disturbances in the stream of evenly spaced droplets – the smaller the droplets, the more often this happens. Occasionally, this will lead to the collision of two droplets some distance away from the orifice.

When two drops of diameter D_d collide, the diameter of the new droplet equals

$$D_{d+d} = 2\sqrt[3]{2\left(\frac{D_d}{2}\right)^3} = \sqrt[3]{2}D_d \approx 1.26D_d. \quad (3.2)$$

Indeed, secondary peaks will often appear in diameter histograms at precisely 126% of the peak diameter. As long as the underlying phenomenon is understood and kept under control, these secondary peaks should be no cause for concern during the calibration. Typically, photographs will confirm that a few droplets go astray and collide with others. Since the “real” diameter peaks are easily discerned, the secondary peaks can simply be ignored.

ILIDS

Interferometric Laser Imaging for Droplet Sizing (ILIDS), also known as Interferometric Particle Imaging (IPI) and MSI (Mie Scattering Imaging) is an optical droplet sizing method in which a spray is illuminated by a sheet of laser light and the scattered light is imaged laterally. The laser light is both reflected and refracted by the droplets, such that each droplet produces a pair of apparent "glare points". When seen through a lens away from the focal plane, each pair of glare points—being sources of coherent monochromatic light—appears as an interference pattern which, after falling through a circular aperture, casts an image that is a circular disk of fringes. The spatial frequency of the fringes is (to a very close approximation) linearly related to the particle size. The phenomenon was first described by König et al. [23] and later in greater detail by Glover et al. [24]. Turnkey ILIDS setups for spray characteriziation are now widely available, comprising typically a pulsed Nd:YAG-laser, one or two CCD cameras, a timing circuit, and a piece of image processing software.

4.1 Operating principle

The number of fringes N_{fr} appearing in the image has a simple linear relationship to the droplet diametre D_d:

$$N_{\mathrm{fr}} = \varkappa D_d, \tag{4.1}$$

where $\varkappa$ is a constant derived from the optical configuration:

$$\varkappa = \frac{\arcsin\left(\frac{D_a}{2z}\right)}{\lambda}\left(\cos\frac{\varphi}{2} - \frac{m\sin\frac{\varphi}{2}}{\sqrt{m^2+1-2m\cos\frac{\varphi}{2}}}\right). \tag{4.2}$$

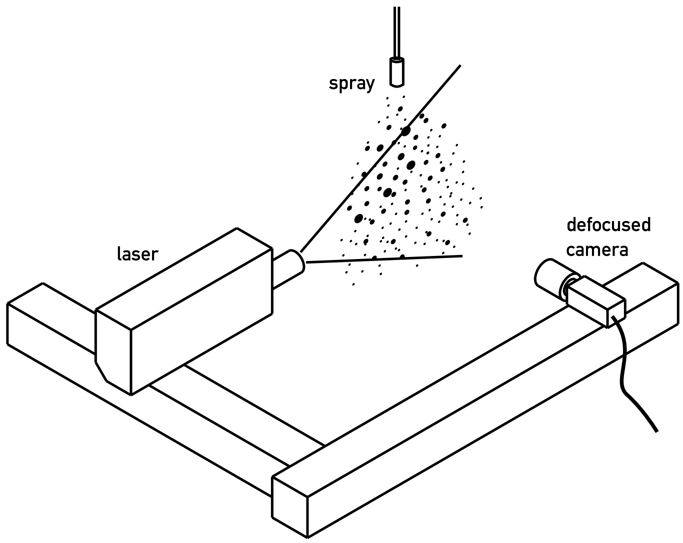

Figure 4.1: Perpendicular ($\varphi = 90°$), single-camera ILIDS setup

In the above expression D_a is the aperture diametre, z is the distance of the lens to the laser sheet, φ is the off-axis angle (90 degrees in most setups, including ours), and m is the relative refractive index of the droplets (1.333 for water in air).

As a consequence of geometrical optics, the distance s_x (in pixels) between two adjacent fringes has a linear relationship with the defocussing distance Δz, where M is the magnification, $d_{p,x}$ is the physical size of a camera sensor pixel, and $\Delta\vartheta$ is the angle subtended by two adjacent fringes entering the lens [25]:

$$s_x = \frac{\Delta\vartheta\Delta z}{M d_{p,x}} \tag{4.3}$$

Of course, equation (4.3) is only meaningful where $\Delta z \gg 0$. When the image is brought into focus ($z \approx 0$), fringes will give way to a sharp image of the glare points.[1] Of course, if the pixel density is too low to resolve both glare points, a single bright spot will appear.

[1]To be exact, diffraction will cause every point to be imaged as an Airy disk, but we shall neglect this effect here.

4.1.1 Influence of the scattering angle φ

The scattering angle φ, illustrated in Fig. 4.2, determines the relative contribution of different scattering orders of light to the imaged fringe pattern. Both geometric optics [26] and Mie theory provide methods to compute the total scattered intensity for a given φ and m; some examples can be found in Kawaguchi et al. [27] and Mounaïm-Rousselle and Pajot [28]. The geometric analysis approach is not valid beyond $\varphi > 70°$, as the first-order scattered beam ($p = 1$) is not visible from this angle [24].

While authors have identified several forward angles as optimal for their applications, e.g. $\varphi = 45°$ [24] or $\varphi = 66°$ [28], such configurations inevitably result in a variation in z, and therefore defocusing, across the image unless the camera itself is angled with respect to the lens to correct for this aberration (the so-called *Scheimpflug condition*). Since the latter approach requires specialized optical equipment, $\varphi = 90°$ is used in many setups, including the one in this paper.

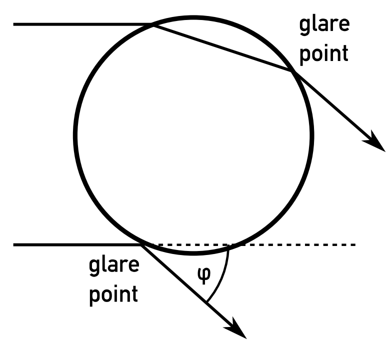

Figure 4.2: Reflected and first-order-refracted light rays, producing two glare points when viewed from an angle φ.

4.1.2 Optical limits on fringe detection

Optics impose theoretical and practical size limits on the droplets to be measured. We will outline them in the following paragraphs; the reader is referred to Damaschke et al. [29] for a more detailed analysis.

Nyquist criterion for the fringe density. The Nyquist criterion requires that for the camera to be able to resolve a pair of neighbouring fringes, their images must be at least two pixels apart. This can easily be achieved by a sufficient defocusing the lens, which widens the fringe image, increasing the number of pixels covered by each fringe. The lens mechanics permitting, any arbitrarily large droplet can thus be measured after a quick adjustment. In theory, this correction is effective until the defocused droplet image is too large for the CCD sensor, and fringes are cut off. In practice, overlap and noise (see below) will cause significant problems long before the image can be defocussed beyond the sensor edges.

Signal-to-noise ratio. Image noise is a significant source of trouble in ILIDS analysis. Indeed, many droplet images must be discarded as data sources because they are too weak compared to the noise. Small droplets suffer from this more than larger ones because they scatter less light,[2] but the problem also occurs with deeply out-of-focus images of very large droplets, as dilated droplet images spread the same amount of light over a greater area on the camera sensor. As a result, they are darker on average than less defocused images.

Minimum droplet size. Damaschke et al. [29] argue that the smallest measurable droplet is one that produces exactly one fringe falling through the aperture. We may speculate that, at least in theory, the fringe frequency should be measurable even if only a partial fringe is shown. This would require its image to be sufficiently zero-padded before the Fourier transform is applied to it. In practice, however, the intensity of scattered light typically drops below an acceptable level well before the fringes become too large, and noise (see above) will become the overwhelming problem.

Deviation from actual Mie scattering for small droplet sizes. ILIDS users should also be aware that the assumptions of geometric optics that underlie (4.2) do not hold for small droplets. Mounaïm-Rousselle and Pajot [28] found that for isooctane droplets ($m = 1.39$) below $10\,\mu$m, geometric optics yield a fringe spacing value about 14% higher than that predicted by exact Mie scattering simulations at $\lambda = 532$ nm. While the deviation quickly vanishes for larger droplets, it is nevertheless noteworthy in the context of potential error sources.

Overlapping droplet images. The ability to image a whole 2D field of droplets all at once is ILIDS' strongest selling point, yet also its curse. When droplets are spaced too closely and the lens is sufficiently defocused, the defocused disk images overlap and it becomes difficult to determine the fringe counts corresponding to individual droplets. Damaschke et al. [29] provide a statistical estimate on the fraction of overlapping disks (overlap coefficient).

[2] The scattered intensity grows with the cross-section of the droplet

4.2 Types of ILIDS setups

4.2.1 Standard ILIDS

The most simple ILIDS configuration, as shown in Fig. 4.1, consists of a single digital camera with a defocused objective lens, placed at a right angle to the laser sheet. The lens aperture is (approximately) circular and typically completely open to permit as much light as possible to fall on the sensor area.

Both camera and laser are connected to a computer via a timing circuit, and both can be triggered simultaneously by software installed on the computer. Commercial ILIDS vendors provide the timing circuitry and the software, which typically integrates a collection of image processing algorithms that can be used to analyze the captured images immediately.

The core problem with all ILIDS setups is the determination of z and d_a in (4.2). We will discuss calibration of ILIDS systems in greater detail in Section **??** calibration.

Images taken in this configuration are very susceptible to excessive disk overlap.

Therefore, measures have been developed to sidestep overlap almost entirely or to deal with it during the image processing stage. These modifications will be described in the next sections.

4.2.2 ILIDS with optical compression

This problem is never more apparent than in efforts to calibrate the system using a vibrating orifice droplet generator, as the droplets produced thereby are spaced very closely and produce heavily overlapping defocussed images. Fortunately, there exists a simple and reliable technique to deal with this problem: a slit aperture, installed directly in front of the lens, masks the defocussed droplet images such that only a thin strip across their center passes through the lens. The effect is shown in Fig. 4.3.

Arguably the most popular way to reduce the amount of overlap is the use of optical compression techniques, whether by means of a slit aperture [25] or a cylindrical lens [27, 30]. However, some techniques (e.g. Global Phase-Doppler [31] and intensity-analyzing methods [32]) or use cases (e.g. very low signal-to-noise ratios) require the full disk image to be available. In these cases, the standard approach is to identify the location and outline of each disk image, such that the fringe analysis can either be limited to non-overlapping regions or be otherwise modified to take overlapping fringes into account.

Naturally, equations (4.2) and (4.3) still hold. Also mention that this can be used in con-

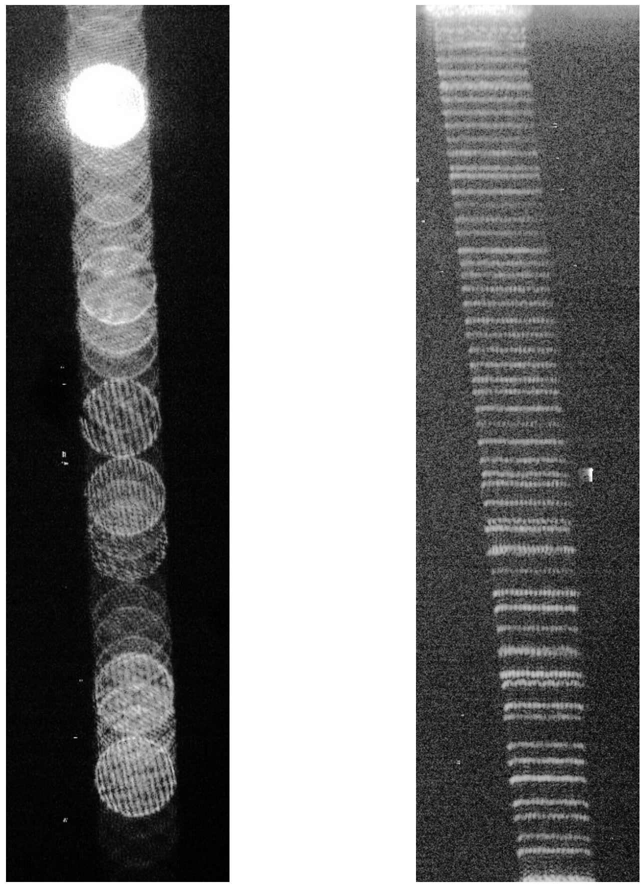

(a) (b)

Figure 4.3: Before (a) and after (b) installing the slit aperture. The aperture stop pares off the top and bottom halves of the defocussed circles, leaving only a narrow center string in the middle.

jecture with an additional, focused camera, to capture things like speed (PIV), evaporation (PLIF), etc. Why we don't need it.

Extracting the fringe counts from such an image is straightforward. First, we correlate the image with that of a single, solid bright rectangle which shares the approximate dimensions of a typical strip in the image. This operation yields intensity peaks centered over our regions of interest. We remove closely adjacent peaks, as they may represent questionable or overlapping strips. Compared to the sheer number of correctly identified strips, the number of legitimate data points lost this way is negligible. Fig. 4.4 shows the result of such an attempt at identifying the strips.

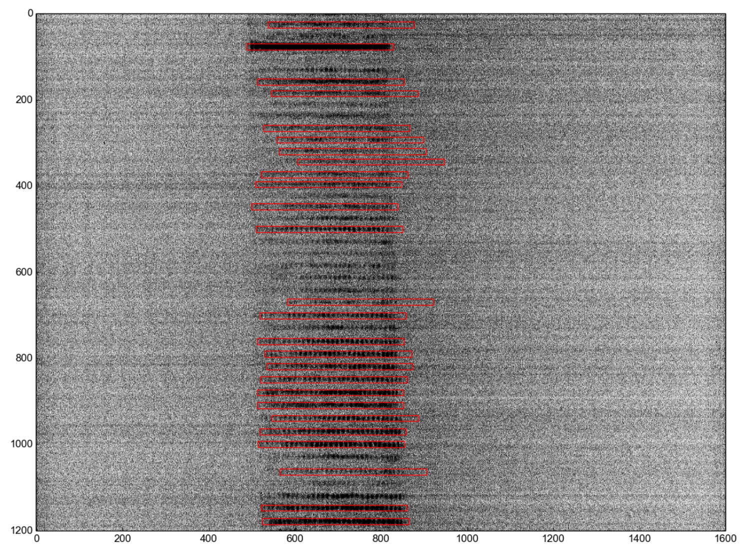

Figure 4.4: The image is correlated with that of a solid bright rectangle, which results in peaks that approximately coincide with the centers of the strips. Here, the original photo is shown with rectangles drawn centered at said peaks.

To find the number of fringes within the strip, we cannot rely on counting the number of dark/bright variations directly, as some of them may be lost in the noise. The spatial frequency of the peaks, however, taken together with the known and constant horizontal width of the strips, will produce a reliable fringe count. In the next step, our algorithm therefore applies the Fourier transform to each region of interest. To improve the accuracy of the method, three steps are performed before the Fourier transform is taken:

1. a weak (3×3) Gaussian blur is applied to the region (optional);

2. a Hanning window is applied to the region – both horizontally and vertically. This reduces the "sinc ringing" effect encountered when taking the Fourier transform of finite signals;

3. the region is padded with zeros in all directions to yield a larger input to the Fourier transform. In our application, the windowed and padded strip images had dimen-

sions of 1024×1024 pixels. Zero-padding increases the granularity of the frequency spectrum, which can help with the correct identification of the peak frequency.

Fig. 4.5 shows the windowed appearance of one such region of interest (although it does not show the padded input to the Fourier transform due to space constraints). The Fourier transform yields a frequency power spectrum in two dimensions, although we are primarily interested in the frequency peak in the horizontal direction (i.e. along $y = 0$). In order to minimize the misidentification of dominant frequencies,

1. we clip the spectrum to a band of reasonable frequencies. This is necessary because a) $1/f$-noise causes very low frequencies to dominate in power, although they are of no interest to us, and b) graininess in the original photo can sometimes result in meritless high-frequency peaks;

2. we apply a Gaussian blur to the 2D spectrum to remove outliers in the spectrum;

3. we discard all regions in which the peak frequency's power does not exceed a certain value;

4. we discard all regions in which the *prominence* of the peak freqency's power (i.e. its proportion to the mean power) does not exceed a certain value (this step is optional).

The bottom two elements in Fig. 4.5 illustrate the effect of these steps.

Finally, the peak frequency f_{peak} is converted into a fringe count by re-scaling it from the padded size D_{padded} ($= 1024$ pixels) to the width of the strip (which, in the context of IPI measurements, should equal the diameter D_{i} of the defocussed droplet image):

$$N_{\text{fr}} = f_{\text{peak}} \frac{D_{\text{i}}}{D_{\text{padded}}} \tag{4.4}$$

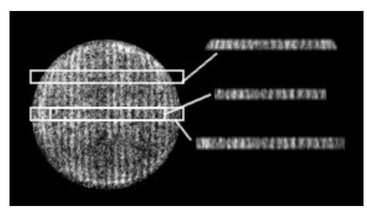

Figure 4.6: Only a slit aperture centered on the lens and extending across the entire lens entrance will preserve all fringes

While the above algorithm will generally give a good estimate of the fringe count for a given defocussed droplet image, it cannot know whether the entire center portion of the image has indeed passed the slit aperture. It is conceivable, after all, that the slit aperture was not perfectly centered on the lens entrance, or that the slit aperture was shorter than the diameter of the lens entrance. Fig. 4.6 illustrates how the slit aperture can cause the defocussed image to appear smaller than it is. The reduced

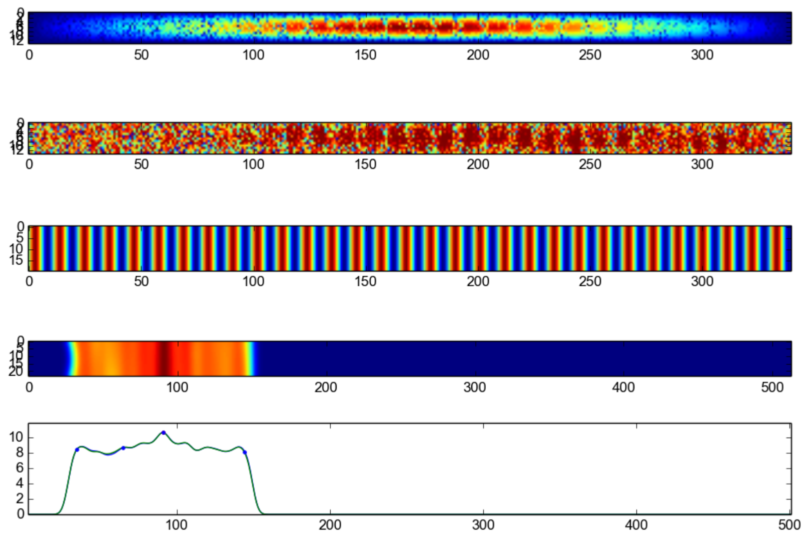

Figure 4.5: From top to bottom: windowed region of interest; original (unwindowed) region of interest; sine wave representing the identified peak frequency; clipped and lowpass-filtered 2D frequency spectrum showing a distinct peak at about 90 oscillations across the image width of 1024 pixels; 1D plot of the frequency spectrum, with peak identified at $f = 91.0$.

value for D_i, manually entered in equation (4.4), will result in droplets being reported as smaller than they are in reality.

As noted above, ILIDS with optical compression can be used with an additional, focused camera behind a beam splitter, as shown in Fig. 4.7.[3] The latter may provide e.g. PIV images for a velocity analysis or LIF images for evaporation studies. This was demonstrated by Hardalupas et al. [33] and Hardalupas et al. [34]. However, such setups suffer from *center discrepancies*. Section 4.5 documents how such center discrepancies can be dealt with.

4.2.3 Additional focused image for disk detection

As described above, running a simple frequency analysis on bright regions in an ILIDS image is futile when two of the fringe disks overlap, as it is not clear how many droplets are associated with the region and where their disks infringe. While optical compression

[3]Alternatively, the two cameras may image the spray from different angles, e.g. as demonstrated by Glover et al. [24], although this complicates the setup as the Scheimpflug condition must be fulfilled.

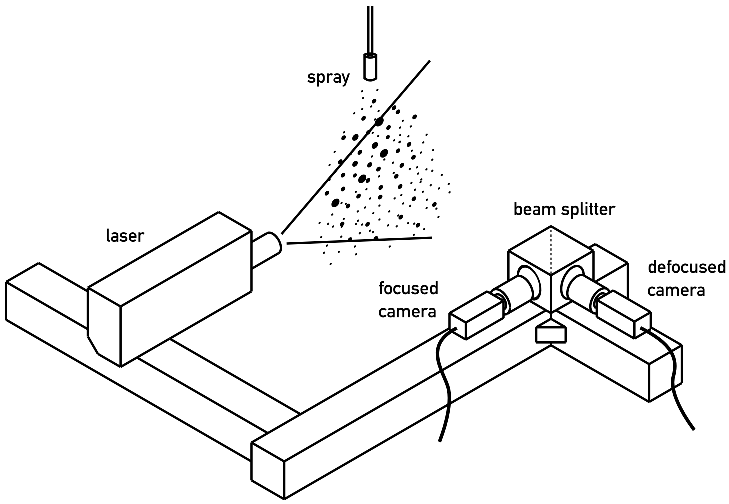

Figure 4.7: Perpendicular ($\varphi = 90°$), double-camera ILIDS setup

provides a very good solution to this problem, it is not always applicable: some techniques (e.g. Global Phase-Doppler [31] and intensity-analyzing methods [32]) or use cases (e.g. very low signal-to-noise ratios) require the full disk image to be available. In these cases, the standard approach is to identify the location and outline of each disk image, such that the fringe analysis can either be limited to non-overlapping regions or be otherwise modified to take overlapping fringes into account. Additionally, once disk centers are found, the software can apply Hanning windows to the disks as well as ignore disk pairs that are too close.[4]

To identify the location of overlapping disks in the image, an additional camera is introduced to capture a focused image of the spray simultaneously with the defocused ILIDS camera. The setup is identical to that shown in Fig. 4.7. The intensity peaks in the focused image are then taken to be the droplet positions (i.e. disk centers) in the defocused image.

The problem with this, as with all multi-camera setups, are center discrepancies. We show how to overcome that in Section 4.4.

[4]The latter is an effective control mechanism, but is liable to skew the representativeness of the sample because small, dispersed satellites outside of the main flow are most likely to be validated.

4.3 Calibrating the slit method

What matters is the Numerical Aperture (NA), which is (the sine of half of) the collection angle. When we have a simple lens, we can calculate this as

$$\mathrm{NA} = \sin\frac{d_a}{2z} \tag{4.5}$$

The Dantec manual suggests using the distance from light sheet to front of the lens for z, and the ratio of min focal length and max f-number to find d_a. This, however, does not result in an accurate value for the collection angle with all lenses.

We are assuming, then, that the effective aperture (the entrance pupil) always stays constant throughout the focussing range of the lens. This is not necessarily the case, as there are lenses which change both the physical and the virtual size of the aperture when focussing.

Here is where I make the claim that it is impossible to determine the actual exact value for the numerical aperture of the lens. Similarly, it can be quite difficult to determine the accurate distance from light sheet to lens aperture (even though the latter measurement is more forgiving, since the distances are far greater).

Taking into account the sources of errors explained in the sections above, it is advisable to run a few calibration tests with droplets of different sizes before employing the IPI technique for real spray measurements. Recall that, if we ignore the Mie error (Section ??), the relationship between fringe count and droplet diameter is linear with a constant of proportionality $\varkappa$ (see equation (4.2)). The aim of our calibration, then, is to determine the value of $\varkappa$ from experiment – the premise being that we cannot be certain of the values of D_a, z, and possibly not even m and φ (although the latter can usually be ascertained to a sufficient degree of accuracy).

4.3.1 A sample calibration of the slit aperture method

Using the droplet generator described in Section 3 and the IPI configuration described in Section 4.2, we produced and measured monodisperse droplets of many different diameters. The droplet diameters were determined both mathematically and photographically, as described in Section ??. Out of over 30 sets of IPI measurements we selected six sets that exhibited both strong uniformity and high photographic quality:

Set	Flow rate	Frequency	D_d, predicted	D_d, from photo	$\hat{N}_{\text{fr}}$
FA	20.8 ml/h	5395 Hz	127 μm	126 μm	9.71
FB	39.7 ml/h	1990 Hz	220 μm	226 μm	16.71
FC	79.4 ml/h	1565 Hz	299 μm	291 μm	22.92
FD	94.3 ml/h	1067 Hz	361 μm	367 μm	27.26
FE	114.1 ml/h	1065 Hz	384 μm	384 μm	29.89
FF	175.2 ml/h	1038 Hz	447 μm	454 μm	34.56

Table 4.1: Six sets of calibration data taken with the setup described in Section 4.2

The values for $\hat{N}_{\text{fr}}$, the peak fringe count, are based on the histograms (see Fig. 4.8) showing the distribution of fringe counts within each dataset. These fringe counts are of course found by the algorithm described in Section **??**.

It is worthwhile to point out some apparent idiosyncrasies in the histograms of datasets FB and FC. Their peak fringe counts are 16.71 and 22.92, but there are secondary peaks at about 21 and 29 fringes, respectively. The latter are explained by the collision of droplets as discussed in Section 3.4.2, and are ignored for the purposes of calibration.

The close agreement of the droplet diameters found from photographs with those predicted by (**??**) reassures us that we can use the predicted D_d for further analysis.

At this point, we can least-squares-fit the linear relationship (4.2) to the primary peaks $\hat{N}_{\text{fr}}$ and the known droplet diameters D_d to find $\hat{\varkappa}$:

$$\hat{\varkappa} = \frac{\sum_i D_{d,i} \hat{N}_{\text{fr},i}}{\sum_i D_{d,i}^2} \tag{4.6}$$

Note that instead of the standard least squares regression we here use a simplified formula to force the trend line through the origin. This choice should not be made lightly, since it will usually cause the residuals to have a non-zero mean. In this case, however, we believe it to be justified to require that $D_d = 0$ for $N_{\text{fr}} = 0$.

Based on the values in Table 4.1, we thus arrive at a value of $\hat{\varkappa} = 76808.1$ with an R^2-value of 99.98%.

Fig. 4.9 illustrates the good agreement on $\varkappa$ between all datasets. Considering the sheer number of error sources – from the unavoidable non-uniformity of the generated droplets to the uncertainty that comes with taking the Fourier transform of a noisy image – the calibration results documented here are a testament to the practical robustness of the method.

It must be remembered, of course, that the peak fringe count values $\hat{N}_{\text{fr}}$ forming the ba-

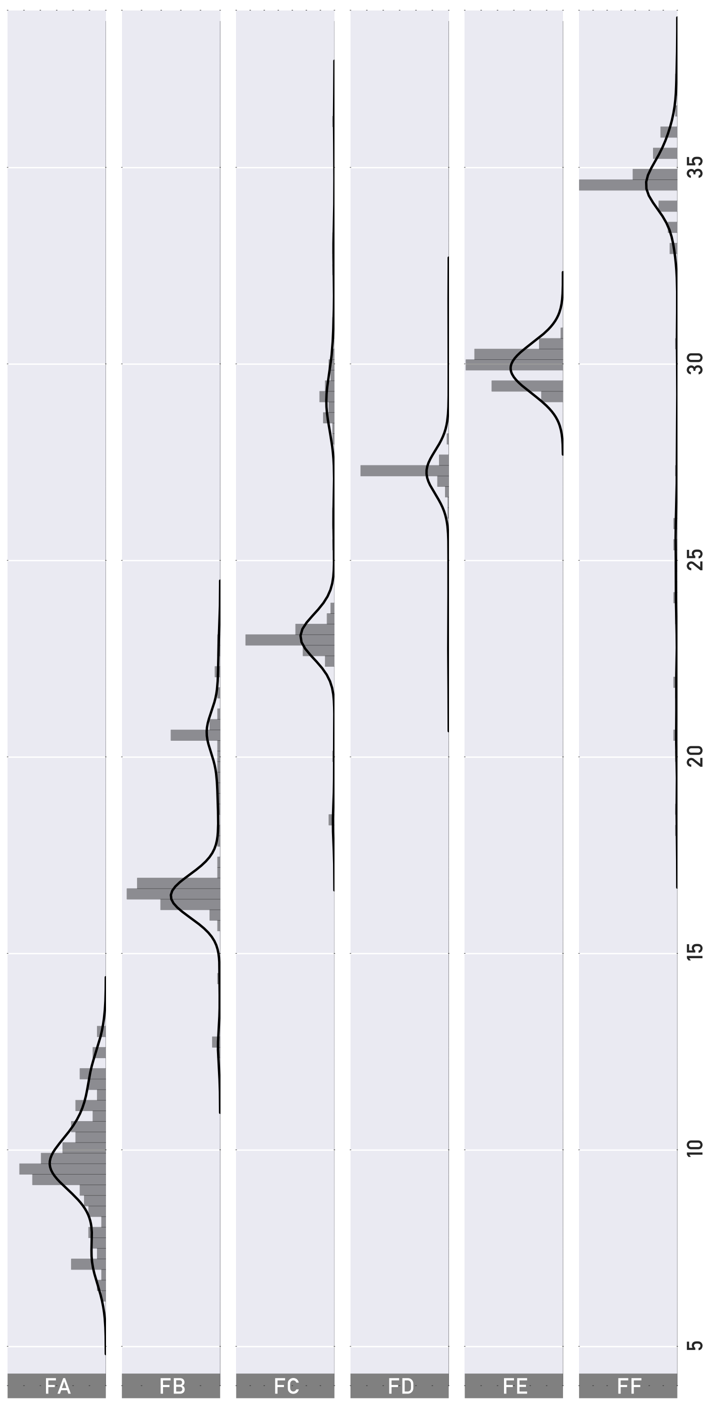

Figure 4.8: Normalized distributions of measured fringe counts N_{fr} for the six datasets listed in Table 4.1. Solid lines are Gaussian kernel density estimates with $h = 0.5$.

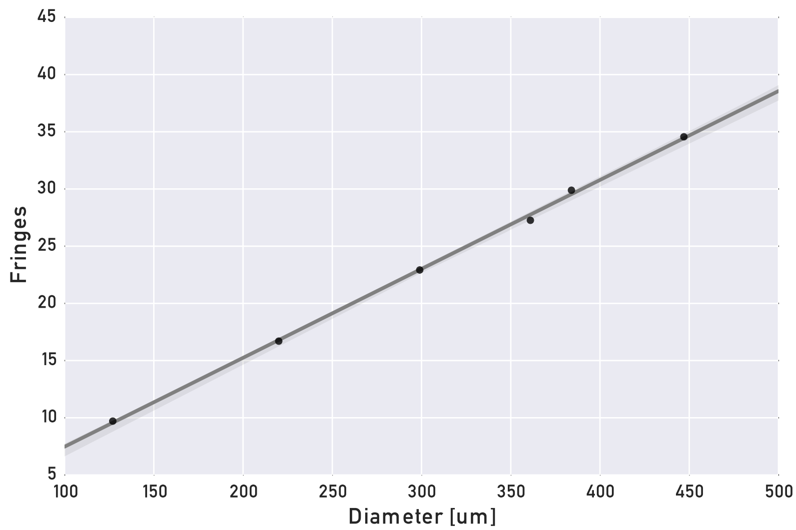

Figure 4.9: Scatterplot of Table 4.1 showing the peak fringe counts $\hat{N}_{\mathrm{fr}}$ for each predicted droplet diameter D_d

sis of our calculation are taken from the peaks of Gaussians fitted to the raw fringe count histograms (see Fig. 4.8. In other words, it is our assumption that all droplets from a given dataset produce fringe counts that are normally distributed around their respective $\hat{N}_{\mathrm{fr}}$. The histogram to dataset FA shows a much higher deviation than the others – this may be due to genuine variance in the generated droplet diameters or to difficulty in processing comparatively weak images with low fringe counts. It seems likely that both effects contribute.

We can compare the empirically determined value $\hat{\varkappa}$ with the mathematical result obtained from (4.2). Substituting $\lambda = 532$ nm, $m = 1.3324$ and $\varphi = 90°$, we conclude that

$$\frac{D_a}{z} = 2\sin\left(\frac{\hat{\varkappa}\lambda}{\cos\frac{\varphi}{2} - \frac{m\sin\frac{\varphi}{2}}{\sqrt{m^2+1-2m\cos\frac{\varphi}{2}}}}\right) = 2\sin(3.11982\cdot 10^{-7}\hat{\varkappa}) \tag{4.7}$$

so for $\hat{\varkappa} = 76808.1$, $\frac{D_a}{z} = 0.047921$. Recall that this quotient is a measure of the collection angle and closely related to the numerical aperture NA= $\sin\frac{D_a}{2z}$. If needed, we can now use this result to compute the input parameters D_a and z in the DantecStudio IPI software:

given, for instance, $z = 45.0$ cm, we can obtain the entrace pupil diameter as

$$0.047921 \cdot 450\,\mathrm{mm} = 2.156\,\mathrm{mm} \tag{4.8}$$

4.4 Removing center discrepancies with keypoint registration

As mentioned above, to allow both cameras to image the same physical region in the spray, they are either placed behind a beamsplitter at a right angle to the light sheet, or placed separately at different angles. The latter approach makes for a more difficult setup, since Scheimpflug's rule demands that the camera must be tilted with respect to the objective lens, but it gives the user the freedom to choose the highest-intensity scattering angle.

In any of the above cases, the use of two cameras requires that their images be mapped onto one another. This is commonly achieved by means of a camera calibration procedure, in which a target pattern (e.g. as in Fig. 4.10) of known dimensions is photographed by each camera. A pattern recognition algorithm then determines the object-to-image mappings for each camera:

$$\begin{bmatrix} x' \\ y' \\ z' \\ r' \end{bmatrix} = \begin{bmatrix} S_x & A_{yx} & A_{zx} & T_x \\ A_{xy} & S_y & A_{zy} & T_y \\ A_{xz} & A_{xy} & S_z & T_z \\ P_x & P_y & P_z & S_0 \end{bmatrix} \begin{bmatrix} x \\ y \\ z \\ 1 \end{bmatrix}. \tag{4.9}$$

In our case, Dantec supplied a *standard dot target*, a white $10 \times 10\,\mathrm{cm}^2$ plate engraved with a pattern of black dots. The plate is to be mounted such that its surface coincides perfectly with the laser sheet.

In practice, $P_{x,y,z} = 0$ and $S_0 = 1$ is assumed, such that the mapping is affine. The z-components (third row/column) are further assumed to be zero, such that a 3×3 matrix suffices for the purposes of this discussion:

$$\begin{bmatrix} x' \\ y' \\ r' \end{bmatrix} = \begin{bmatrix} S_x & A_{yx} & T_x \\ A_{xy} & S_y & T_y \\ P_x & P_y & S_0 \end{bmatrix} \begin{bmatrix} x \\ y \\ 1 \end{bmatrix}. \tag{4.10}$$

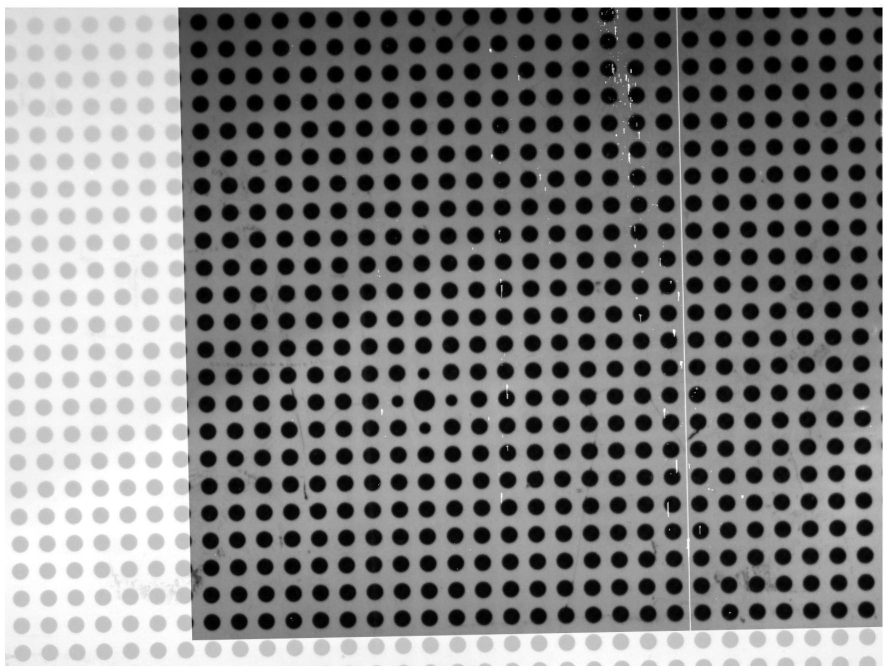

Figure 4.10: Homography **H** applied to target pattern image captured by the focused camera and superimposed on the image captured by the defocused camera (here, both cameras were in focus for the calibration only).

The calibration algorithm thus finds the camera matrices $\mathbf{P}_{\text{foc}}$ and $\mathbf{P}_{\text{def}}$ mapping the object coordinates $\mathbf{x}$ onto the two camera images $\mathbf{x}'_{\text{foc}}$ and $\mathbf{x}'_{\text{def}}$ (the respective subscripts shall hence designate the focused and defocused cameras):

$$\mathbf{x}'_{\text{foc}} = \mathbf{P}_{\text{foc}}\,\mathbf{x} \tag{4.11}$$

$$\mathbf{x}'_{\text{def}} = \mathbf{P}_{\text{def}}\,\mathbf{x}. \tag{4.12}$$

It follows that the quotient of the two matrices, also known as the homography

$$\mathbf{H} = \mathbf{P}_{\text{def}}\,\mathbf{P}_{\text{foc}}^{-1} \tag{4.13}$$

can be used to map the focused image onto the defocused image, as shown in Fig. 4.10:

$$\mathbf{H}\,\mathbf{x}'_{\text{foc}} = \mathbf{x}'_{\text{def}}. \tag{4.14}$$

Unfortunately, the calibration procedure itself introduces an unwanted distortion: to capture a viable photo of the target pattern, the defocused camera must be temporarily brought into focus, as was done in Fig. 4.10. This is not mentioned e.g. in the application manual of Dantec's IPI system, but is a practical necessity. Bringing a camera out of focus not only introduces a blur, it also scales the image extents. Fig. 4.11, adapted from Hardalupas et al. [33], shows schematically how this effect creates "center discrepancies". Since the extents of the defocused image are either smaller or larger than those of the focused image, depending on the direction of defocusing, all droplet images are projected either closer to or farther away from the image center. The discrepancy is worst for droplets far away from the image center. As a result, the centers of objects in simulatenously captured focused and defocused images no longer align (Fig. 4.12), and the calibration procedure becomes self-defeating.

While this error is easy to account for in the ideal case of right angles and perfect alignments (simply rescaling the image would solve the problem) the situation becomes more difficult in practice when the target pattern is no longer parallel to the camera sensor (intentionally or accidentally) or when cylindrical lenses are used to add optical compression. In fact, there is no guarantee that affine mappings are sufficient in the general case.

Surprisingly, only Hardalupas *et al.* [33, 34] have hitherto published a discussion of this effect, and the only previous mention known to the authors is in Kurosawa et al. [35], who dismissed it as a "positioning error".

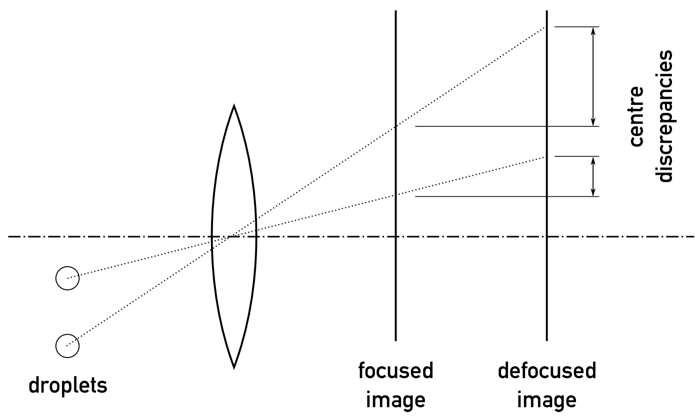

Figure 4.11: Schematic showing the source of center discrepancies in the case of parallel image and object planes

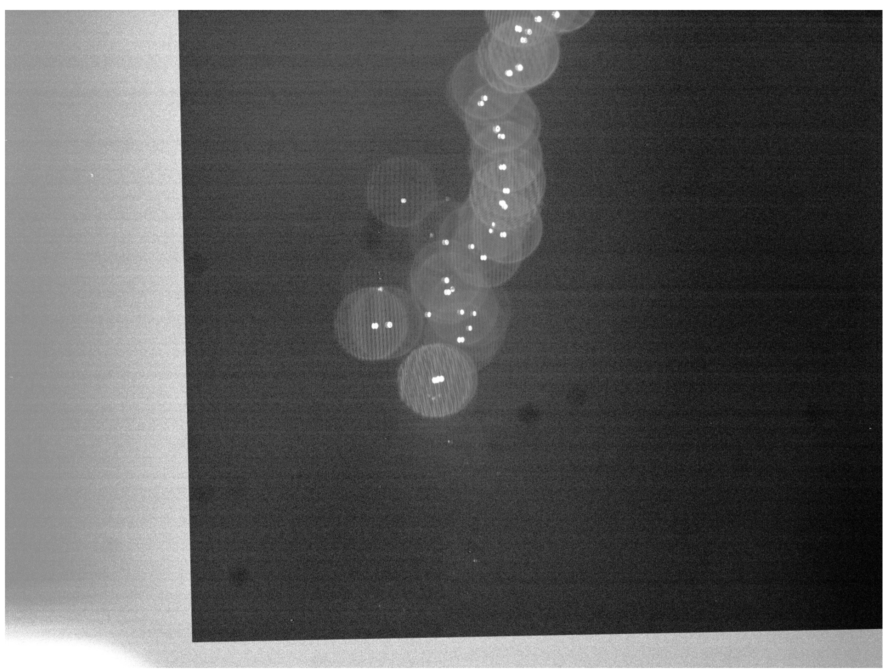

Figure 4.12: Focused camera image, after applying homography **H** derived from the calibration images, is superimposed onto defocused camera image of droplets. Discrepancies between object centers grow towards the edge of the image.

Hardalupas *et al.* identified the centers of particles in both PIV (focused) and ILIDS (defocused) images. They then empirically estimated the magnitude of the center discrepancy effect along the vertical axis, which enabled them to improve the accuracy of their nearest-neighbour-based droplet image matching algorithm.

We found that algorithms developed by the computer vision community in recent years can obviate the need for calibration entirely. Instead, we can use visual correspondences between the focused and defocused images to find the mapping between them directly. To that end, we first provide in Section 4.4.1 a brief overview over popular methods in the field of automated (linear) *registration*, i.e. the art of finding a *homography* (geometric mapping) between two *epipolar images* (images of the same object, taken from different positions and angles). Section **??** documents our approach in greater detail and shows the result of a successful recalibration.

4.4.1 Review of image registration techniques

Given two identical images that have been rotated, shifted or even scaled with respect to one another, the applied transformation can theoretically be found by means of a brute-force search. This method is not feasible in practice, not only because of its enormous computational complexity (there are no gradients to guide the search) but also because of its inability to deal with noise, focal blur, perspective changes and other nonlinearities introduced by the photographic process. Conversely, normalized cross-correlation measures between images, as commonly used in PIV, are unaffected by noise but not invariant to rotation and scale and therefore not generally practical. The standard approach to image registration is therefore a three-step process. First, *keypoints*, i.e. "interesting" points in the images are found by a keypoint detection algorithm. Then, a small image patch at every keypoint is extracted and converted into a *feature vector*, a set of numbers providing a very general description of the image patch that accounts for scale, rotation, blur, contrast, etc. Finally, matches between similar feature vectors from the two images are found, outliers are removed, and the homography is calculated.

However, the results of a keypoint detection algorithm must be as repeatable as possible, i.e. the same set keypoints should be found in both images regardless of their relative position, rotation, scale, etc. For instance, the Harris corner detector [36], one of the earliest keypoint detectors, is sensitive to scale and thus often unusable.

The recent decade has seen a rapidly growing collection of proposed keypoint detectors, beginning with SIFT [37], SURF [38] and BRISK [39], all of which include keypoint extractors, to CENSURE [40], optimized for speed, and FAST [41], which incorporates machine learning methods. Finally, the recent publication of ORB [42] includes a rotation-aware version of FAST used in this paper. Many more have been developed but are not included here for brevity's sake.

Keypoint extractors (sometimes called *descriptors*) are often optimized for and therefore included with keypoint detectors, as in the instances mentioned above. Some however are standalone algorithms, such as BRIEF [43].

It is straightforward to find matching keypoints by searching for pairs with the smallest arithmetic distance between their feature vectors (e.g. using the L^2 norm). This nearest-neighbour search can be done exhaustively in linear time to find the optimal matching, but many faster, if approximate, search methods exist. We should note FLANN [44], a publicly available collection of such implementations which includes a fully automatic parameter selection heuristic.

Finally, the homography, assuming one exists, can be derived from the set of matched keypoint coordinate pairs. Since many of the found matches will be wrong, it is of essence to use a robust estimator, i.e. a type of regression model designed to ignore outliers. Possibly the oldest of these methods is RANSAC [45], an iterative procedure in which sets of data points are chosen at random and discarded if the agreement between a model fit to them and all other data points falls below a carefully chosen threshold. RANSAC was used for this paper, although other robust methods exist. The criterion developed by Moisan and Stival [46] deserves special mention in our context; it does away with RANSAC's hard threshold and instead takes into consideration the probability of a match to be in consensus with epipolar geometry.

4.4.2 Using affine oriented FAST, BRIEF and RANSAC to estimate the homography between PIV and ILIDS photographs

Existing PIV/ILIDS systems derive the homography from the result of a camera calibration procedure which the user is required to perform before analyzing images. Although the final value of $\mathbf{H}$ is invisible to the user in our copy of Dantec's DynamicStudio software, the camera matrices $\mathbf{P}_{\text{foc}}$ and $\mathbf{P}_{\text{def}}$ can be shown and edited. We therefore must find a corrected homography $\hat{\mathbf{H}}$ that allows us to compute

$$\hat{\mathbf{P}}_{\text{def}} = \hat{\mathbf{H}}\,\mathbf{P}_{\text{foc}} \tag{4.15}$$

so that we can replace $\mathbf{P}_{\text{def}}$ with $\hat{\mathbf{P}}_{\text{def}}$ in the software, effectively correcting $\mathbf{H}$ to $\hat{\mathbf{H}}$.

To efficiently extract keypoints, we combined three algorithms: ASIFT [47] to deal with skew transformations; an oriented version of FAST, published as part of ORB, to detect keypoints; and standard BRIEF as a keypoint extractor.

ASIFT is a method originally developed to be used with SIFT. It introduces invariance to affine mappings by simulating various projective transformations while FAST and BRIEF are run repeatedly. This slows the analysis down, but given the infinitude of possible angled camera-camera-object configurations, it is wise to maintain a flexible framework.

We should note that the original ASIFT with SIFT works well, but SIFT is encumbered by patents. To encourage vendors of imaging systems to adopt the proposed algorithms, we made it our goal to find a freely available replacement.

Recall that the disks in the defocused image are missing from the focused image, rendering a registration between them impossible. It is straightforward to simulate the disks, however. We followed the following protocol on our focused images:

1. Mask the image, blacking out all areas that are known not to contain droplets.

2. Subtract the pixel-wise minimum or mean value taken over all images taken by the camera. This step serves to black out defective hot pixels on the camera's CCD and other static noise.

3. Erode the image, using a 3×3 or 5×5 kernel. This will close any remaining bright pixels which are likely noise.

4. Locate the intensity peaks in the remaining image.

5. Fill a blank image with black, then draw bright circles of diameter D_{disk} onto it, centerd at the respective positions of the intensity peaks detected in the focused image. (Note that simply dilating the result of the previous step will not lead to circular disks.)

The result of performing these operations on our sample image is shown in Fig. 4.13. We determined the disk diameter D_{disk} empirically from the defocused images, although it

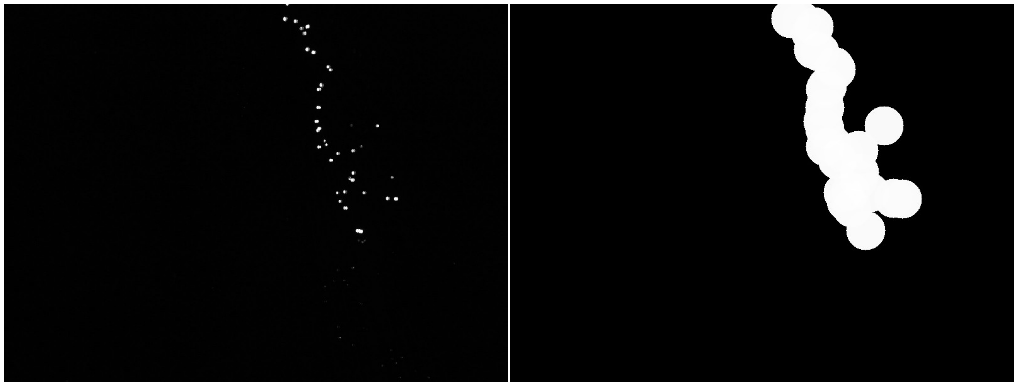

Figure 4.13: Simulating disks based on the focused image.

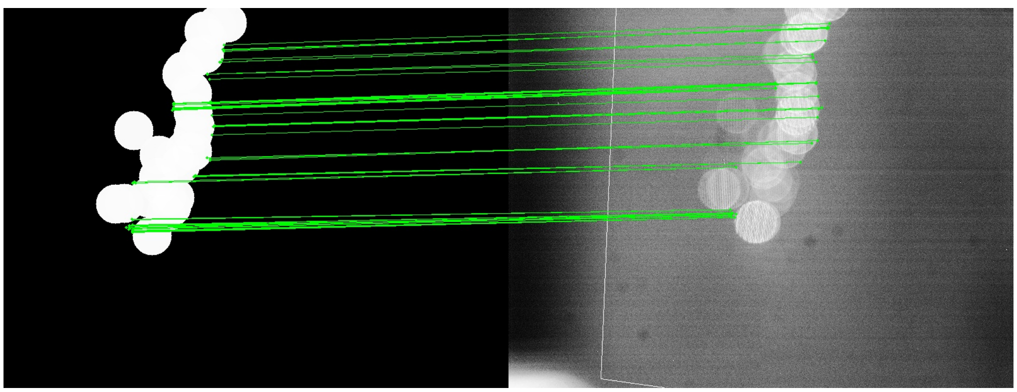

Figure 4.14: Visualized inliers in the set of matched keypoints between the mirrored simulated disks (see Fig. 4.13) and the ILIDS image.

is naturally preferable to automate this step, e.g. using circular Hough transforms or cross-correlation with circular masks. There may be simpler ways of achieving the same result, e.g. by means of Gaussian filters, distance transforms and thresholding operations. However, we found the protocol described above to be quite robust to noise and fast enough for our application.

Implementations of ORB and BRIEF are freely available through the OpenCV project, which provides bindings for the C++ and Python languages. We used these implementations to find and extract matching keypoints between our sample images, shown in Fig. 4.14.

The matches shown in Fig. 4.14 were found using a most basic method: brute-force match search, followed by a RANSAC estimation of the homography matrix $\mathbf{K}$ using a threshold of 10.

Since the two cameras were positioned behind a beamsplitter in our setup, the defocused image was flipped horizontally. We therefore first mirrored it horizontally, using the transformation matrix

$$\mathbf{M}_h = \begin{bmatrix} -1 & 0 & \text{(image width)} \\ 0 & 1 & 0 \\ 0 & 0 & 1 \end{bmatrix}.$$

To speed up the image registration process, it can be helpful to first down-scale the images. To reduce an image to half of its original size, apply

$$\mathbf{S}_{0.5} = \begin{bmatrix} 0.5 & 0 & 0 \\ 0 & 0.5 & 0 \\ 0 & 0 & 1 \end{bmatrix}.$$

While the above operations might not be strictly necessary, we found that they significantly improved the quality of the matches identified. If the registration algorithms mentioned above now find a homography matrix $\mathbf{K}$, then we can write

$$\mathbf{K}\,\mathbf{M}_h\,\mathbf{S}_{0.5}\,\mathbf{P}_{\text{foc}} = \mathbf{S}_{0.5}\mathbf{P}_{\text{def}} \tag{4.16}$$

and to bring this into a form similar to (4.14),

$$\begin{aligned} \mathbf{S}_{0.5}^{-1}\,\mathbf{K}\,\mathbf{M}_h\,\mathbf{S}_{0.5}\,\mathbf{P}_{\text{foc}} &= \mathbf{S}_{0.5}^{-1}\,\mathbf{S}_{0.5}\mathbf{P}_{\text{def}} && (4.17) \\ &= \mathbf{P}_{\text{def}} && (4.18) \end{aligned}$$

Finally, it turns out that Dantec's DynamicStudio software violates convention by placing the coordinate origin at the bottom (not top) left corner of the image. We must therefore pre- and post-multiply by $\mathbf{M}_v^{\pm 1}$, with

$$\mathbf{M}_v = \begin{bmatrix} 1 & 0 & 0 \\ 0 & -1 & \text{(image height)} \\ 0 & 0 & 1 \end{bmatrix},$$

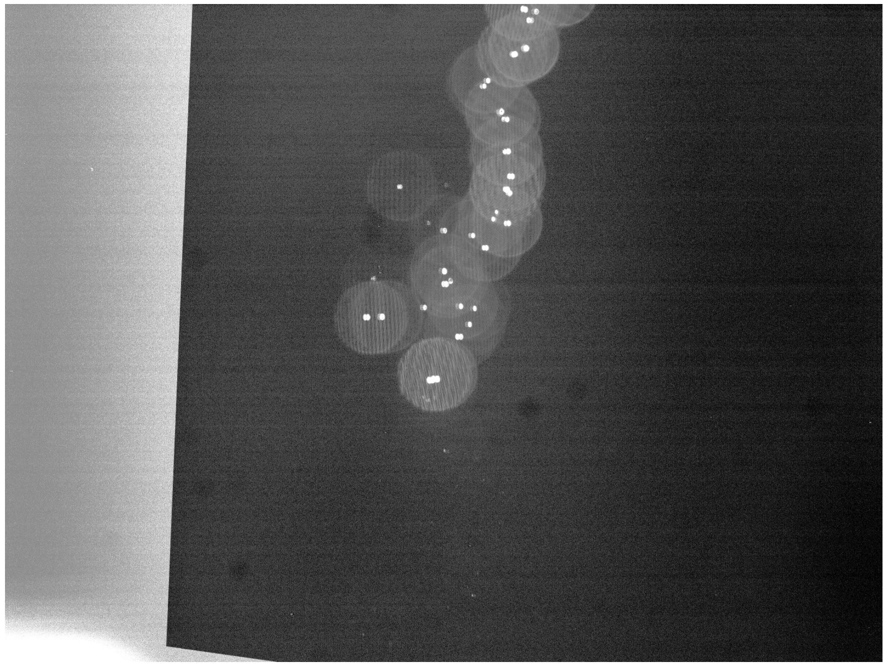

Figure 4.15: Focused camera image, after applying corrected homography $\hat{\mathbf{H}}$ derived from the matched keypoints, is superimposed onto defocused camera image of droplets.

to arrive at our final expression for $\hat{\mathbf{H}}$:

$$\hat{\mathbf{H}} = \mathbf{M}_v \, \mathbf{S}_{0.5}^{-1} \, \mathbf{K} \, \mathbf{M}_h \, \mathbf{S}_{0.5} \, \mathbf{M}_v^{-1}. \tag{4.19}$$

Substitution of $\hat{\mathbf{H}}$ into (4.15) yields $\hat{\mathbf{P}}_{\text{def}}$, which can be manually entered into the DynamicStudio software. Fig. 4.15 illustrates how the use of $\hat{\mathbf{H}}$ leads to an improved alignment compared to Fig. 4.12. Note that a slight projective distortion is necessary for optimal registration, confirming that it is infeasible to restrict the homography to affine matrices.

4.5 Removing center discrepancies with point set registration

The keypoint matching approach described above is not applicable when a slit aperture was used to reduce overlap, as in the paper by Hardalupas *et al.*, so we will outline briefly how to use registration algorithms with such setups.[5]

Keypoints are not required, when the absence of overlap allows us to identify focused and defocused objects centers directly from the respective images and find a projection mapping between them. Indeed, Hardalupas *et al.* successfully registered their PIV and ILIDS images that way: using wavelet transforms at various frequencies, they identified the putative droplet centers on both focused and defocused images. Then, using a continuous, single-stream monodisperse droplet generator, they estimated how the magnitude of the center discrepancies varied over the image. After applying this empirically estimated distortion to the captured focused images, they matched each focused droplet to the closest defocused droplet (if one could be found within an subjectively chosen search distance).

Although they reported good success using this method, it requires both an empirical estimation of the center discrepancies every time the camera is defocused *and* a guess at the appropriate search window size. Moreover, mismatches are likely as the naive closest-neighbour search is not robust to noise. To eliminate these steps, we suggest that droplet matches be found directly using a robust point set registration algorithm.

Since the early 1990s, computer vision researchers have accumulated an impressive body of work on this topic, most of it focusing either on rigid transformations (i.e. translation and rotation only) or non-rigid transformations (typically understood to include nonlinear warping). The problem at hand requires an algorithm able to deal with projective transforms, which are non-rigid but linear.

The only paper known to the authors to specifically address this case is by Chi et al. [48], who propose an iterative search based on image moments. Since image moments are an aggregate metric, they do not directly lead to a droplet-to-droplet correspondence. Still, closest-neighbour matches after application of this algorithm would likely produce results no worse than those found after estimating the transformation empirically.

Robust non-rigid methods are also applicable in this case and deserve some mention. Many of them are probabilistic relaxations of the Iterative Closest Point algorithm, which simply searches for the least-squares-optimal rigid mapping. Several of these approaches were reviewed and generalized by Jian and Vemuri [49]. A slightly different approach, named Coherent Point Drift[50], is also highly popular and illustrated in Fig. 4.16.

We forgo at this point a documentation of the application and refer the reader to Hardalupas *et al.*, who describe their center identification technique in good detail, and to the

[5] While slit strip images could be simulated over the focused image (in a procedure analogous to that illustrated in Fig. 4.13), the lack of overlap between them could make it significantly more difficult to find "interesting" keypoints in the simulated image.

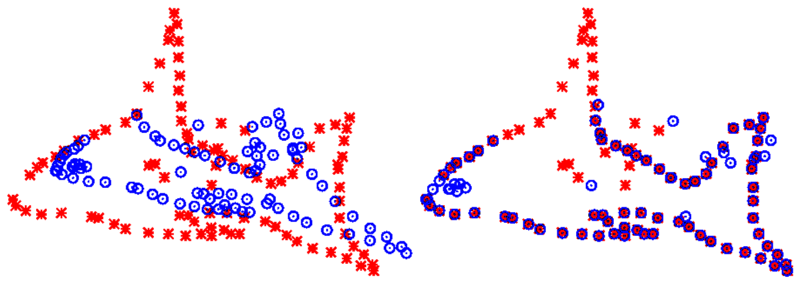

Figure 4.16: Non-rigid variant of the Coherent Point Drift algorithm applied to two point sets. Notice that the probabilistic nature of the matching creates robustness to unmatched points. (Image source: Wikipedia)

above-mentioned authors, who have published freely available implementations of their algorithms online.

Phase-Doppler Particle Analysis (PDPA)

Phase-Doppler anemometry and droplet sizing techniques are based on the far-field intensity fluctuations in the laser light scattered by passing droplets. Unlike ILIDS, however, PDPA uses intersecting laser beams (instead of a laser sheet) to illuminate the droplets. Whereas ILIDS *images* the infringement pattern cast by the glare points on the illuminated droplet, PDPA measures the fringe spacings indirectly by relating them to the phase difference between the signals recorded by a pair of adjacent detectors.

Doppler [51] proposed in 1842 that the slight differences in wavelength between the colours of various stars could be used to determine the stars' velocities relative to Earth. A century later, military radar operators during World War II realized that the Doppler effect could be exploited to estimate target velocities using their radar systems. Soon, meteorologists had adopted the technology to measure wind speeds [52]. The flurry of activity around Doppler measurements in the ensuing years produced the first laser-based particle anemometry system, designed in 1964 by Yeh and Cummins [53], and several novel beam-detector configurations have been proposed since. Among them are the popular dual-beam configurations, constitutiting a departure from the original reference beam systems which can be more difficult to align. A exemplary dual-beam setup is shown in Fig. 5.1.

Laser-Doppler anemometry (LDA, also known as laser-Doppler velocimetry or LDV) provides velocity measurements only. The 1970s saw the discovery that the fringe patterns cast by the scattered light could be analyzed to yield size information [54, 55]. This technique is now widely used and often integrated into the detecting and processing hardware of commercial LDA systems, typically under the name of phase-Doppler Anemome-

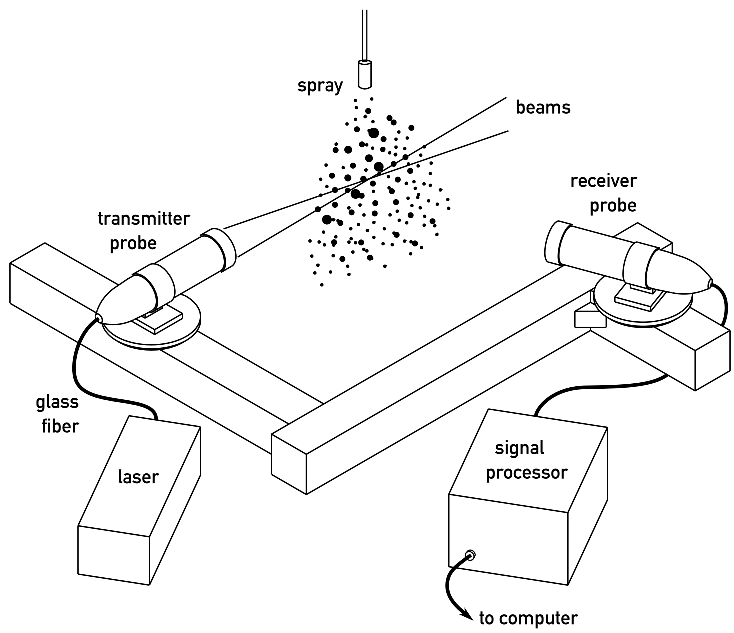

Figure 5.1: Typical commercial PDPA configuration using transmitter and receiver probes

try (PDA) or phase-Doppler particle analysis (PDPA).

PDPA can be used to ascertain droplet size distributions with a very high precision. Nevertheless, its accuracy hinges on the knowledge of a large number of distances, angles and voltages. A single erroneous one of them will throw off the result, leaving the operator none the wiser.

5.1 Optical principle

The two beams, coming from top and bottom, create two glare points at 30 deg (30 deg off-angle). The two glare points cause a moving pattern of dark and bright fringes. The pattern is picked up by both receivers, both of which record a modulated sinusoid as the droplet falls past them.

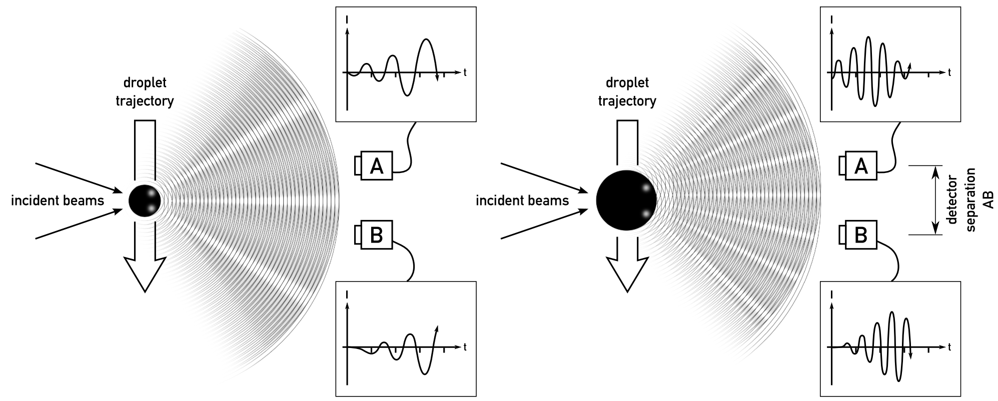

Figure 5.2: Moiré-style visualization of the interference pattern cast by the two glare points. Left: glare points on small particles are close, resulting in wide fringes. The signals recorded by detectors A and B are shifted in time by a phase difference $\Delta\Phi_{AB}$, which is due to the detectors' known separation in space. Right: glare points on larger particles are farther apart, resulting in narrower fringes and a larger phase difference.

5.2 Sources of error

5.2.1 Gaussian beam divergence

The theory predicting the linear relationship between detector phase difference and droplet diameter is founded on the assumption of very small droplets and plane beam wavefronts. **(Question: is it the wavefront curvature or the non-uniformity of the intensity that causes problems?)**

The problem is termed *trajectory ambiguity effect* (TAE) or *Gaussian beam defect* (GBD) in the literature.

This phenomenon was recognized first by Saffman [56] but had to be neglected until the plane-wave scattering theory of Lorenz-Mie optics was extended into the *Generalized Lorenz-Mie Theory* (GLMT). Most of this work was done by Gouesbet, Gréhan, Maheu, Lock and others throughout the 1980s [57, 58, 59, 60], and mathematically rigorous formulations were available by the early 1990s [61, 62]. The 1996 paper by Gouesbet and Gréhan summarizes these developments and provides an early overview over the attempts to circumvent the TAE [63]. More discussion is given e.g. by

Solutions are a) a planar setup, b) double-burst measurements, c) epsilon validity measurements. It is important to align the receiver properly; the tables used by TSI were developed using GLMT by Naqwi and Menon [64].

5.2.2 Slit effect

Durst et al show experimentally that the slit effect is even more crucial than the Gaussian beam effect. [65]. Together with the TAE, this is called the measurement volume effect. Qiu and Hsu propose using four detectors, instead of three, to resolve this problem entirely [66]. A similar design was verified experimentally by Sipperley and Bachalo [67].

A more recent review of the phenomenon and associated techniques was given by Strakey et al. [68**?**].

5.2.3 Change in fringe frequency over z

The curved wavefront causes the fringe spacing to vary along the axis of the measurement volume. At the near and far ends of the volume, the fringes are spaced wider, which can result in an error on the order of 10%. (Red Book)

5.2.4 Selection of lenses and masks

Davis and Disimile talk about the TAE only tangentially. They provide results of the same spray using different masks and focal lengths [69].

5.2.5 Optical aberrations

See Dressler and Kraemer [21].

5.2.6 Wrongly entered parameters

The optical principle involves many more geometric parameters than are needed for the operation of ILIDS or laser diffraction (Malvern) devices. As a result, an excellent interface and a very attentive user are required to ensure accurate results.

In practice, I always get error messages when doing the last step, and the values are way out of the expected range. The result, then, is that the D20 is made very close to the expected monodisperse diameter. Since the D20 is quite a bit larger than the actual (and completely obvious) peak value, even these ”wrong” values aren’t correct.

5.3 Calibration

Calibration is tricky, because

knowndiam = argmax(gaussian(average(diamAB[within7percent], diamAC[within7percent])))

Since the selection of droplets with <=diff(diam) and the gaussian kernel density estimate are one-way functions, it's impossible to work backwards. We also want to minimize the angle in the difference-diameter plot, i.e. the PCA is supposed to be as close as possible to 0 and 90 degrees. So the only way to do this reliably is to iterate over the two AB and AC values to find an optimum.

Nonetheless, even with this method the relationship between the distance values AB and AC is typically linear, and once the linear relationship has been found, we can find the combination of values that produces the most straight PCA and the most centered cluster. Let's approximate the

Breakup of a water jet when colliding with an air jet

We built an angle plate like this:

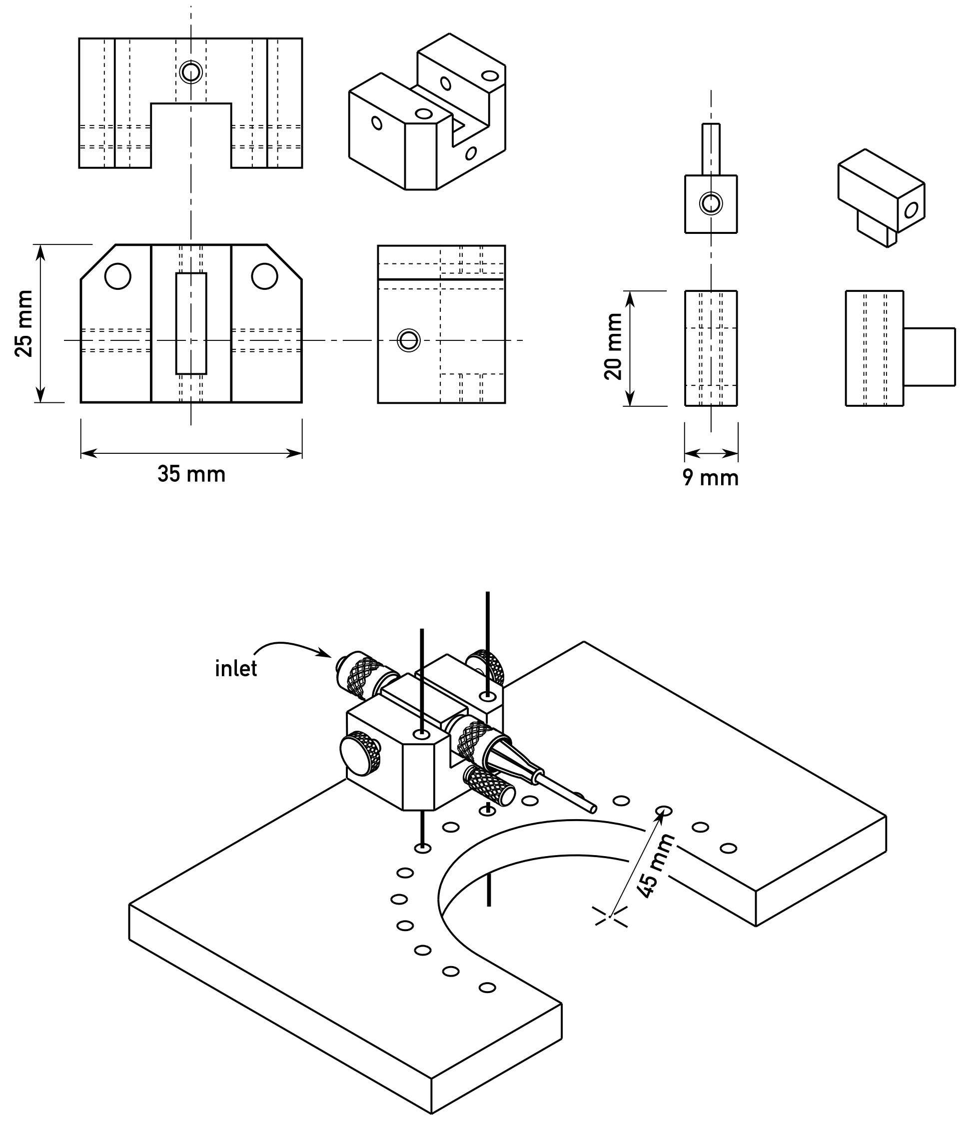

Figure 6.1: Angle plate setup

Bibliography

[1] W. H. Walton and W. C. Prewett. The production of sprays and mists of uniform drop size by means of spinning disc type sprayers. *Proceedings of the Physical Society B*, 62: 341–350, Jun 1949.

[2] C. R. Merritt and J. A. Drinkwater. A laboratory device for producing single drops in uniform sizes of 150–450 μm diameter. *Pesticide Science*, 8:457–562, 1977.

[3] C. R. Allan, H. R. Carlon, A. K. Stuempfle, T. E. Hoffer, and R. L. Pitter. Survey of the literature: Controlled generation of liquid droplets. Technical Report TR-88164, Chemical Research, Development & Engineering Center, U.S. Army Munitions Chemical Command, Aug 1988.

[4] W. R. Lane. A microburette for producing small liquid drops of known size. *Journal of Scientific Instruments*, 24:98, Apr 1947.

[5] K. Reil and J. Hallett. An apparatus for the production of uniform sized water drops, at desired time intervals. *Review of Scientific Instruments*, 40:533–534, Apr 1969.

[6] S. Coggins and E. A. Baker. Micro sprayers for the laboratory application of pesticides. *Annals of Applied Biology*, 102:149–154, Feb 1983.

[7] W. J. Stry. *The combustion of free flowing droplets of chlorinated benzenes, alkanes, and their mixtures*. PhD thesis, SUNY Buffalo, September 1992.

[8] I. Endo, Y. Sato, S. Saito, T. Nakagiri, and S. Ohno. Bubble jet recording method and apparatus in which a heating element generates bubbles in a liquid flow path to project droplets, February 2 1988. US Patent 4,723,129.

[9] A. V. Sergeyev and R. A. Shaw. An inexpensive uniform-size aerosol generator. *Measurement Science and Technology*, 17:N41, 2006.

[10] J. C. Yang, W. Chien, M. King, and W. L. Grosshandler. A simple piezoelectric droplet generator. *Experiments in Fluids*, 23:445–447, 1997.

[11] H. Ulmke, T. Wriedt, and K. Bauckhage. Piezoelektrischer Tropfengenerator zur Kalibrierung von Partikelzählern. *Chemie Ingenieur Technik*, 71(12):1387–1391, 1999.

[12] H. P. Le. *Progress and trends in inkjet printing technology*, volume 42.

[13] E. Lee. *Microdrop Generation*. Nano- and Microscience, Engineering, Technology and Medicine. Taylor & Francis, 2002.

[14] A. Amirzadeh Goghari and S. Chandra. Producing droplets smaller than the nozzle diameter by using a pneumatic drop-on-demand droplet generator. *Experiments in Fluids*, 44:105–114, Jan 2008.

[15] G. J. Green, D. E. Walsh, F. Takahashi, and F. L. Dryer. Aerodynamic device for generating mono-disperse fuel droplets. *Review of Scientific Instruments (ISSN 0034-6748)*, 60:646–652, Apr 1989.

[16] F. Savart. Memoire sur la constitution des veines liquides lancees par des orifices circulaires en mince paroi. *Annales de Chimie et de Physique*, 53:337–386, 1833.

[17] L. Rayleigh. On the capillary phenomena of jets. *Proceedings of the Royal Society of London*, 29:71–97, 1879.

[18] R. J. Donnelly and W. Glaberson. Experiments on the capillary instability of a liquid jet. *Proceedings of the Royal Society of London. Series A. Mathematical and Physical Sciences*, 290(1423):547–556, 1966. doi: 10.1098/rspa.1966.0069.

[19] J. M. Schneider and C. D. Hendricks. Source of uniform-sized liquid droplets. *Review of Scientific Instruments*, 35:1349–1350, Oct 1964.

[20] R. N. Berglund and B. Y. H. Liu. Generation of monodisperse aerosol standards. *Environmental Science and Technology*, 7:147–153, Feb 1973.

[21] J. L. Dressler and G. O. Kraemer. A multiple drop-size drop generator for calibration of a phase-doppler particle analyzer. *Liquid Particle Size Measurement Techniques*, 2 (1083):30–44, 1990.

[22] L. Ström. The generation of monodisperse aerosols by means of a disintegrated jet of liquid. *Review of Scientific Instruments*, 40:778–782, Jun 1969.

[23] G. König, K. Anders, and A. Frohn. A new light-scattering technique to measure the diameter of periodically generated moving droplets. *Journal of Aerosol Science*, 17: 157–167, 1986.

[24] A. R. Glover, S. M. Skippon, and R. D. Boyle. Interferometric laser imaging for droplet sizing: a method for droplet-size measurement in sparse spray systems. *Applied Optics*, 34:8409–8421, Dec 1995.

[25] G. Pan, J. Shakal, W. Lai, R. Calabria, P. Massoli, and O. Pust. Simultaneous global size and velocity measurement of droplets and sprays. *Spray '06 – Workshop über Sprays, Erfassung von Sprühvorgängen und Techniken der Fluidzerstäubung*, 2006.

[26] H. van de Hulst. *Light Scattering by Small Particles*. Dover Books on Physics. Dover Publications, 2012.

[27] T. Kawaguchi, Y. Akasaka, and M. Maeda. Size measurements of droplets and bubbles by advanced interferometric laser imaging technique. *Meas Sci Technol*, 13:308–316, Feb 2002.

[28] C. Mounaïm-Rousselle and O. Pajot. Droplet sizing by mie scattering interferometry in a spark ignition engine. *Part Part Syst Charact*, 16:160–168, 1999.

[29] N. Damaschke, H. Nobach, and C. Tropea. Optical limits of particle concentration for multi-dimensional particle sizing techniques in fluid mechanics. *Experiments in Fluids*, 32:143–152, 2002.

[30] M. Maeda, Y. Akasaka, and T. Kawaguchi. Improvements of the interferometric technique for simultaneous measurement of droplet size and velocity vector field and its application to a transient spray. *Experiments in Fluids*, 33:125–134, Jun 2002.

[31] N. Damaschke, S. Rasmussen, C. Tropea, and A. Woite. Global phase doppler technique. In *6th International Congress on Optical Particle Characterisation, Brighton, UK*, 2001.

[32] A. Quérel, P. Lemaitre, M. Brunel, E. Porcheron, and G. Gréhan. Real-time processing algorithm of global interferometric laser imaging for the droplet sizing (ilids) in

airborne research. In *15th International Symposium on Applications of Laser Techniques to Fluid Mechanics*, Jul 2010.

[33] Y. Hardalupas, S. Sahu, A. M. K. P. Taylor, and K. Zarogoulidis. Simultaneous planar measurement of droplet velocity and size with gas phase velocities in a spray by combined ilids and piv techniques. *Experiments in Fluids*, 49:417–434, 2010.

[34] Y. Hardalupas, S. Sahu, and A. M. K. P. Taylor. Measurement of vapour concentration and droplet size and velocity in an evaporative spray. In *15th International Symposium on Applications of Laser Techniques to Fluid Mechanics*, Jul 2010.

[35] R. Kurosawa, K. Hishida, and M. Maeda. Combined measurement of lif and ilids for vapor concentration and droplets size and velocity in a spray. In *11th International Symposium on Applications of Laser Techniques to Fluid Mechanics, Lisbon, Portugal*, 2002.

[36] C. Harris and M. Stephens. A combined corner and edge detector. In *Procedings of the Alvey Vision Conference 1988*, pages 23.1–23.6, Jan 1988.

[37] D. G. Lowe. Distinctive image features from scale-invariant keypoints. In *International Journal of Computer Vision*, volume 60, page 91, Nov 2004.

[38] H. Bay, A. Ess, T. Tuytelaars, and L. V. Gool. Speeded-up robust features (surf). *Computer Vision and Image Understanding*, 110:346–359, 2008.

[39] S. Leutenegger, M. Chli, and R. Y. Siegwart. Brisk: Binary robust invariant scalable keypoints. In *2011 IEEE International Conference on Computer Vision (ICCV)*, pages 2548–2555, 2011.

[40] M. Agrawal, K. Konolige, and M. R. Blas. Censure: Center surround extremas for realtime feature detection and matching. In *10th European Conference on Computer Vision*, pages 102–115, 2008.

[41] E. Rosten and T. Drummond. Fusing points and lines for high performance tracking. In *2005 IEEE International Conference on Computer Vision (ICCV)*, volume 2, pages 1508–1515, 2005.

[42] E. Rublee, V. Rabaud, K. Konolige, and G. Bradski. Orb: an efficient alternative to sift or surf. In *2011 IEEE International Conference on Computer Vision (ICCV)*, pages 2564–2571, Nov 2011.

[43] M. Calonder, V. Lepetit, C. Strecha, and P. Fua. Brief: Binary robust independent elementary features. In *11th European Conference on Computer Vision*, volume LNCS 6314, pages 778–792, 2010.

[44] M. Muja and D. G. Lowe. Fast approximate nearest neighbours with automatic algorithm configuration. In *International Conference on Computer Vision Theory and Applications*, pages 331–340, Feb 2009.

[45] M. A. Fischler and R. C. Bolles. Random sample consensus: A paradigm for model fitting with applications to image analysis and automated cartography. *Communications of the ACM*, 24:381–395, Jun 1981.

[46] L. Moisan and B. Stival. A probabilistic criterion to detect rigid point matches between two images and estimate the fundamental matrix. *International Journal of Computer Vision*, 57:201–218, 2004.

[47] J.-M. Morel and G. Yu. Asift: a new framework for fully affine invariant image comparison. *SIAM Journal on Imaging Sciences*, 2:438–469, 2009.

[48] Y.-T. Chi, J. Ho, and M.-H. Yang. A direct method for estimating planar projective transform. In *10th Asian Conference on Computer Vision*, pages 268–281, 2011.

[49] B. Jian and B. C. Vemuri. Robust point set registration using gaussian mixture models. *IEEE transactions on pattern analysis and machine intelligence*, Dec 2010.

[50] A. Myronenko and X. Song. Point set registration: coherent point drift. *IEEE transactions on pattern analysis and machine intelligence*, 32:2262–2275, Dec 2010.

[51] C. Doppler. Über das farbige licht der doppelsterne und einiger anderer gestirne des himmels. *Abhandlungen der k. böhm. Gesellschaft der Wissenschaften*, 5:465–482, 1842.

[52] R. C. Whiton, P. L. Smith, S. G. Bigler, K. E. Wilk, and A. C. Harbuck. History of operational use of weather radar by u.s. weather services. part ii: Development of operational doppler weather radars. *Weather and Forecasting*, 13:244–252, 1998.

[53] Y. Yeh and H. Z. Cummins. Localized fluid flow measurements with an he-ne laser spectrometer. *Applied Physics Letters*, 4:176–178, May 1964.

[54] F. Durst and M. Zare. Laser Doppler measurements in two-phase flows. In P. Buchhave, J. M. Delhaye, F. Durst, W. K. George, K. Refslund, and J. H. Whitelaw, editors,

The Accuracy of Flow Measurements by Laser Doppler Methods, Proceedings of the LDA-Symposium '95, Copenhagen, Denmark, pages 403–429, 1976.

[55] G. Wigley. The sizing of large droplets by laser anemometry. *Journal of Physics E: Scientific Instruments*, 11:639–642, 1978.

[56] M. Saffman. The use of polarized light for optical particle sizing. In *Proceedings of the 3rd International Symposium on Applications of Laser Anemometry to Fluid Mechanics, Lisbon, Portugal*, page 18.2, 1986.

[57] G. Gréhan, G. Gouesbet, and C. Rabasse. The computer program supermidi for lorenz-mie theory and the research of one-to-one relationships for particle sizing. In *Proceedings of the symposium on long range and short range optical velocity measurements*, Institut franco-allemand de Saint-Louis, September 1980.

[58] G. Gouesbet and G. Gréhan. Sur la généralisation de la théorie de lorenz-mie. *Journal of Optics*, 13(2):97–103, 1982.

[59] G. Gouesbet, B. Maheu, and G. Gréhan. Light scattering from a sphere arbitrarily located in a gaussian beam, using a bromwich formulation. *Journal of the Optical Society of America A*, 5(9):1427–1443, 1988.

[60] B. Maheu, G. Gouesbet, and G. Gréhan. A concise presentation of the generalized lorenz-mie theory for arbitrary location of the scatterer in an arbitrary incident profile. *Journal of Optics*, 19(2):59–67, 1988.

[61] J. A. Lock and G. Gouesbet. A rigorous justification of the localized approximation to the beam shape coefficients in generalized lorenz-mie theory, i. on-axis beams. *Journal of the Optical Society of America A*, 11(9):2503–2515, 1994.

[62] G. Gouesbet and J. A. Lock. A rigorous justification of the localized approximation to the beam shape coefficients in generalized lorenz-mie theory, ii. off-axis beams. *Journal of the Optical Society of America A*, 11(9):2516–2525, 1994.

[63] G. Gouesbet and G. Gréhan. Gaussian beam errors in phase-doppler anemometry and their elimination. In R. Adrian, D. Durão, F. Durst, M. Heitor, M. Maeda, and J. Whitelaw, editors, *Developments in Laser Techniques and Applications to Fluid Mechanics*, pages 243–259. Springer Berlin Heidelberg, 1996.

[64] A. Naqwi and R. Menon. A rigorous procedure for design and response determination of phase doppler systems. In *Proceedings of the 7^{th} International Symposium on Applications of Laser Anemometry to Fluid Mechanics, Lisbon, Portugal*, pages 340–353, 1994.

[65] F. Durst, C. Tropea, and T.-H. Xu. The slit effect in phase doppler anemometry. In *Modern techniques and measurements in fluid flows: Proceedings of the 2nd International Conference on Fluid Dynamic Measurement and Its Applications*, Oct 1994.

[66] H. Qiu and C. T. Hsu. Method of phase-doppler anemometry free from the measurement-volume effect. *Applied Optics*, 38(13):2737–2742, May 1999.

[67] C. M. Sipperley and W. D. Bachalo. Triple interval phase doppler interferometry: Improved dense sprays measurements and enhanced phase discrimination. In *17th International Symposium on Applications of Laser Techniques to Fluid Mechanics, Lisbon, Portugal*, Jul 2014.

[68] P. A. Strakey, D. G. Talley, S. V. Sankar, and W. D. Bachalo. Phase Doppler Interferometry with Probe-to-Droplet Size Ratios Less Than Unity. Part I: Trajectory Errors. *Applied Optics*, 39(22):3875–3886, Aug 2000.

[69] J. M. Davis and P. J. Disimile. The effect of optical configuration selection on phase doppler anemometer fire suppressant nozzle characterizations. In *14th Halon Options Technical Working Conference*, May 2004.